Optical Modulation and Spectroscopy with Silicon Microspheres

by

Emre Yüce

A Thesis Submitted to the
Graduate School of Sciences and Engineering
in Partial Fulfillment of the Requirements for
the Degree of

Master of Science

in

Physics

Koç University

July 2009

Koç University

Graduate School of Sciences and Engineering

This is to certify that I have examined this copy of a master's thesis by

Emre Yüce

and have found that it is complete and satisfactory in all respects,
and that any and all revisions required by the final
examining committee have been made.

Committee Members:

_____

Ali Serpengüzel, Ph. D. (Advisor)

_____

Özgür Müstecaplıoğlu, Ph. D.

_____

Oğuzhan Gürlü, Ph. D.

Date: _____

ABSTRACT

Remarkable amount of research is being devoted to the merger of microelectronics and microphotonics on a single silicon chip. Additionally, substantial amount of research has demonstrated a variety of optical functionalities for microspheres. Possessing high quality factor morphology dependent resonances, microspheres have been investigated in resonant cavity enhanced optoelectronic applications. Silicon microspheres, combining the advantage of both the spherical shape and the optoelectronic properties of silicon are ideal candidates for integrated photonics. In this work, silicon microspheres have been excited in the S-band using optical fiber half couplers. The transmission spectra and the elastic scattering spectra from a silicon microsphere have been obtained. Potential difference is applied to the silicon microsphere using two gold electrodes placed on the reciprocal sides of the silicon microsphere. Optical modulation has been observed in both the transmitted and the 90^{o} elastic scattered spectra for the transverse electric and transverse magnetic polarizations. The applied voltage at increasing duty cycles provided promising results about the spectral signature of the morphology dependent resonances.

ÖZET

Çağımızda mikroelektroniğin ve mikrooptiğin tümleşik devre üzerinde birleştirilmesi için araştırmalar yapılmaktadır. Önemli miktarda araştırma mikroyuvarların çeşitli optik özelliklerini bildirmiştir. Yüksek kalitedeki yapı tabanlı çınlamalara sahip olan mikro-yuvarlar gelişmiş çınlaç uygulamaları için araştırılmıştır. Hem yuvarlak bir yapıya sahip olmaları hem de üstün optoelektronik özellikleri ile silisyum mikroyuvar geleceğin tümleşik devre fotonik uygulamalarında kullanılmak için güçlü bir adaydır. Bu çalışmada silisyum mikroyuvarlar optik dalga kılavuzu kullanılarak, S-bandında iletim ve esnek saçılma izgeleri gözlemlenmiştir. Daha sonra yuvarın iki karşıt tarafında bulunan altın elektrodlar kullanılarak yuvara gerilim uygulanmıştır. Elektriksel sinyal yardımıyla optik ayarlama, elektrik ve manyetik kutuplaşımlar için hem iletim izgesinde hem de esnek saçılma izgesinde gözlemlenmiştir. Buna ek olarak değişik çalışma zamanlı elektriksel sinyal kullanılarak yuvarın yapı tabanlı çınlamalarının izgesi gözlemlenmiştir.

ACKNOWLEDGEMENTS

I would like to express my gratitude to my M.Sc. thesis advisor, Professor Ali Serpengüzel, for the support and guidance he provided me throughout my study.

I would like to thank to my thesis committee members Professor Özgür Müstecaplıoğlu and Professor Oğuzhan Gürlü for reading my thesis and providing constructive feedback.

I am deeply grateful to our group members, Hasan Yılmaz, Mohammed Sharif Murib and David Kurt Webb for valuable discussions.

I would like to thank my friends Abdurrahman Turgut, Aziz Ömeroğlu, Fatih Baltacı, Fatih Yoğurtçu, Gürkan Turan, Gökhan Turan, Orhan Özdemir, Saltuk Buğra Tanfer, Selçuk Dağ, Sertan Kutal Gökçe, Sinan Azak, and Yunus Eren for their friendship, which has been the support I needed during my research in Koç University Microphotonics Research Laboratory.

In addition, I would like to thank to my parents for their love, support, advice, and patience they provide during my life. Moreover, I would like to thank to my fiancée, Eda Cihangirli for her love, and support, which will be the building block of my future.

Lastly, I would like to acknowledge Türkiye Bilimsel ve Teknolojik Araştırma Kurumu (TÜBİTAK) grant No. EEEAG 106E215 and European Commission (EC) grants No's FP6-IST-003887 NEMO and FP6-IST-511616 PHOREMOST for their financial support to our research.

This thesis is dedicated to my parents.

TABLE OF CONTENTS

LIST OF TABLES

LIST OF FIGURES

NOMENCLATURE

a	Microsphere radius
a_n	Elastically scattered transverse magnetic field coefficient
b_n	Elastically scattered transverse electric field coefficient
c_n	Internal transverse magnetic field coefficient
d_n	Internal transverse electric field coefficient
E	Electric field amplitude
e	Unit charge
$\hbar$	Plank's constant divided by 2π
$h_n^1(x)$	Spherical Hankel function of the first kind
$h_n^2(x)$	Spherical Hankel function of the second kind
$j_n(x)$	Spherical Bessel function
k	Wave vector
k	Imaginary part of the refractive index
L	Spreading length of the Gaussian Beam
l	Radial mode order
m	Angular mode number
m	Relative refractive index
m_0	Electron mass
m_{ce}	Conductivity effective mass of electrons
m_{ch}	Conductivity effective mass of holes
N	Concentration of free carriers
N_e	Concentration of electrons
N_h	Concentration of holes
n	Polar angular mode number

s	Beam confinement parameter of the Gaussian Beam
ω	Optical angular frequency
$\omega_{n,l}$	Resonant angular frequency
p	Momentum of the photon
P_i	Power coupled into an MDR
Q	Charge
Q	Quality factor of a MDR
Q_o	Quality factor associated with the internal losses
$Q_{coupling}$	Quality factor associated with the coupling losses
Q_{abs}	Quality factor associated with the absorption losses
Q_r	Quality factor associated with the diffraction losses
Q_s	Quality factor associated with the scattering losses
x	Size parameter of the microsphere
$\Delta\lambda$	Mode spacing in wavelength
$\delta\lambda$	Wavelength shift
ε	Permittivity of the medium
θ	Polar angle
θ_{in}	Angle of incidence
θ_c	Critical angle
λ	Wavelength of light in vacuum
$\Delta\lambda_{1/2}$	Linewidth of an MDR
μ	Permeability of the medium
ν	Frequency
$\Delta\nu_{1/2}$	*Linewidth in frequency*

Chapter 1

INTRODUCTION

The need for low cost photonic devices, high-speed intrachip and interchip communication, and high bandwidth, low power consumption and interference free connections in conventional microelectronics are some of the reasons for investigating optoelectronic integrated circuits. Silicon is a relatively inexpensive, well-understood, naturally abundant, mass producible material for fabricating microelectronic integrated circuits [1]. Moreover, silicon is transparent in the optical telecommunication bands and therefore highly suitable for passive and active optoelectronic devices [2]. Researchers already demonstrated the observation of the stimulated Raman scattering (SRS) [3] in crystalline silicon waveguides.

Additionally, substantial amount of research has demonstrated a variety of optical functionalities for microspheres [4]. Possessing high quality factor morphology dependent resonances (MDR's), microspheres [5] have been investigated in resonant cavity enhanced (RCE) optoelectronic applications [6]. Using polymer [7] and silicon nanocrystal [8] coated silica microspheres optical switching has been demonstrated. Additionally, silicon modulators [9] have been developed first using a metal-oxide-semiconductor (MOS) capacitor [10], a Mach-Zehnder [11] configuration, SRS [12], and a microring [13] configuration, a microracetrack configuration [14], a p-i-n diode based microdisk [15], a p-n diode on a silicon waveguide [16], and a photonic crystal [17]. Silicon microspheres, combining the advantage of both the spherical shape and the optoelectronic properties of silicon are ideal candidates for integrated photonics.

Chapter 2 gives brief information about the optical resonators by describing Fabry-Perot resonators. Later the microsphere resonators, which are the 3D version of the Fabry-

Perot resonators, are discussed. The Lorenz-Mie theory is also discussed in order to give the necessary background.

Chapter 3 describes the optical modulation techniques for silicon. The effect of the applied electric field on absorption coefficient and refractive index are discussed. Later, the carrier injection effect, which gives rise to absorption coefficient and reduces the refractive index, is discussed. Thermo-optical effect, which is competing with the electro-optical effect, is discussed. Moreover, all optical modulation is studied.

Chapter 4 starts with the theory of the metal semiconductor contact. Later the experimental setup and the electrical properties of the device are demonstrated with the relevant IV measurements during applied dc and ac electrical signal to the silicon microsphere.

In chapter 5, the modulated optical spectra in transmission and in 90^0 elastic scattering with the applied voltage are shown. Then the modulation performed at different duty cycles are shown in order to demonstrate the relevant shift in MDR's with the applied voltage. Lastly, the spectral signature of the MDR's during the optical modulation is presented in this chapter.

This thesis is concluded with the summary of the performed study as well as possible future work in chapter 6. In the appendix, the virtual instruments developed by using LabView® are given.

Chapter 2

OPTICAL RESONATORS

2.1. Introduction

Confined light navigating inside a closed space with a negligible loss might build up a strong electric field, if a constructive interference occurs. This constructive interference occurs only at definite wavelengths. These wavelengths, can be interpreted as the modes of the resonator. Resonators have been built in one dimension using planar and spherical mirrors. Light has been confined in two dimensions by using microring [18], microtoroid [19], and microdisk [20] resonators. Moreover, light has been confined in three dimension using microsphere resonators [21]. Eq. 2.1 gives the general condition for all the resonators. Eq. 2.1 states that in a round-trip, the light should satisfy the phase matching with the incident beam, such that the phase difference of the incident light and that of the traveled light should constructively interfere by a multiple of 2π.

$$\delta = 2\pi n \qquad (2.1),$$

where n is the integer mode number. The waves satisfying phase matching condition interfere constructively, resulting in a series of standing electromagnetic waves. The corresponding modes determine the resonant wavelengths of the resonator. The radiation energy is stored in these modes at the definite wavelengths.

2.2 The Fabry-Perot Resonator

A Fabry-Perot resonator consists of two parallel mirrors with high reflectance. If the mirrors are fixed the resonator is called an etalon. On the other hand, if the resonator length is variable, the resonator is called an interferometer. A schematic of a Fabry-Perot resonator is shown in Fig. 2.1. The incident light is coupled inside the resonator and bounces back from the second mirror. The second mirror with a high reflectivity transmits only a little portion of the light. Then the light comes back to the first mirror and bounces back again as well. During this round trip light interferes with itself. If this interference is constructive then a strong electric field is formed inside the resonator. At the resonance wavelengths the light is transmitted regardless of the high reflectance of the mirror. These wavelengths of the incident light satisfying the resonance condition in eq. (2.1) are called the resonance wavelengths.

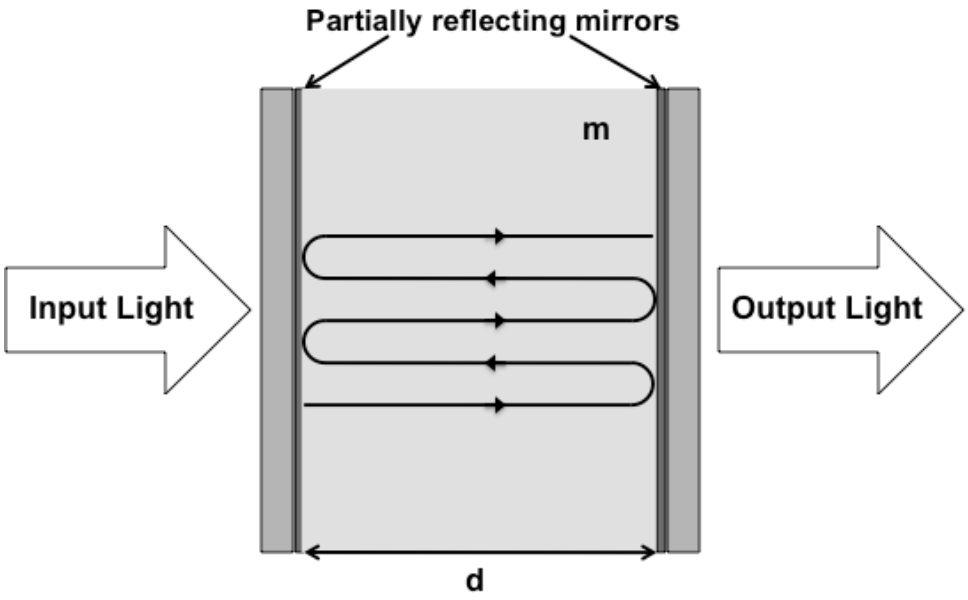

Figure 2.1. The schematic of the Fabry-Perot resonator.

2.2.1 Resonator Modes

The solution to the Helmholtz equation with the appropriate boundary conditions can be interpreted as the modes of a resonator. A mode is a self-reproducing wave that interferes with itself constructively within the resonator, and only self-reproducing waves can exist inside the resonator. Resonant wavelengths are defined with the solution of the equation for standing waves for a Fabry-Perot resonator. Eq. 2.2 gives the standing wave solution.

$$n\frac{\lambda_n}{2} = md \qquad (2.2),$$

where m is the refractive index of the medium, d the spacing between the two plates, λ the vacuum wavelength of the light, and n an integer mode number. We can define a dimensionless size parameter (x) as the ratio of the round-trip length to the wavelength of the incident light in order to simplify the Eq. 2.2,

$$x = \frac{2d}{\lambda} \qquad (2.3).$$

Using Eq. 2.3 in Eq. 2.2, we can obtain the following relation between the mode number n and the refractive index of the medium m (Eq. 2.4).

$$mx = n\,, \qquad n = 1, 2, 3, \ldots \qquad (2.4),$$

The waves satisfying Eq. 2.1 interfere constructively, which results in a series of standing electromagnetic waves given by Eq. 2.4. Taking the derivative of Eq. 2.2 and dividing it with itself, we can find the sensitivity of the resonator. In fact, the sensitivity of the resonator (Eq. 2.5) is the shift in a resonance wavelength caused by the change in the

resonator length or the refractive index of the medium. Moreover, Eq. 2.5 also states that the resonance wavelength can be chosen by changing the size or the refractive index of the resonator.

$$\delta\lambda = \lambda\left(\frac{\delta d}{d} + \frac{\delta m}{m}\right) \tag{2.5}.$$

The quality factor (*Q-factor*) of the resonator is defined by the Eq. 2.6. *Q-factor* of a resonator gives information about the sensitivity and the resolving power of a resonator.

$$Q = 2\pi \frac{stored\ \ energy}{energy\ \ loss\ \ per\ \ cycle} \tag{2.6}.$$

The *Q-factor* can be interpreted as the ratio of the wavelength to the full width at half maximum (FWHM) of the resonance. The FWHM of a resonance is shown as $\Delta\lambda_{1/2}$ in the spectra given in Fig. 2.2

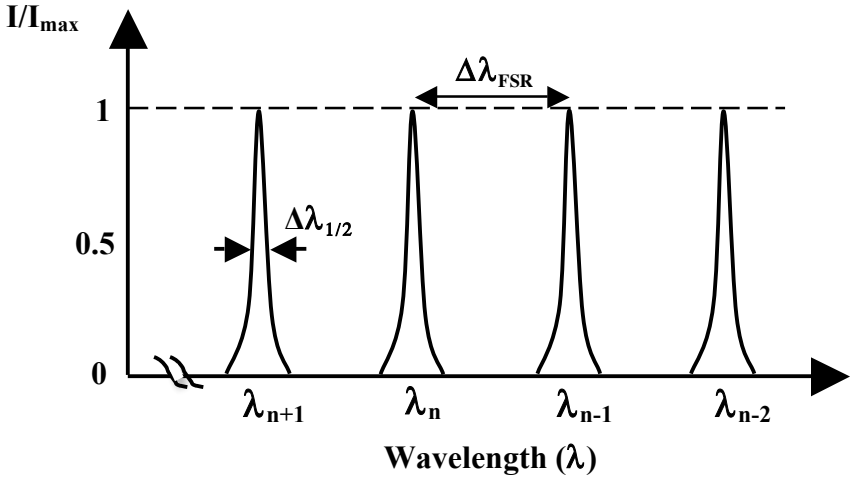

Figure 2.2. A schematic of the transmitted light intensity spectrum.

The *Q-factor* for a resonator can be obtained by replacing the energy loss per cycle with $\Delta\lambda_{1/2}$ and approximating the stored energy as the center wavelength λ (Eq. 2.7).

$$Q = \frac{\lambda}{\Delta\lambda_{1/2}} \tag{2.7}$$

Using the relation c= λν, we can write the *Q-factor* in frequency domain (Eq. 2.8).

$$Q = \frac{\upsilon}{\Delta\upsilon_{1/2}} \tag{2.8}$$

The wavelength selectivity of a resonator increases with the *Q-factor* and the *Q-factor* of a resonator increases with the reflectance of the mirrors. In fact, the higher the reflectance the higher the energy stored inside the resonator. Moreover, the sharpness of the resonance peaks will increase with the increasing reflectance.

The separation between the resonance peaks is given by the free spectral range (FSR), which is also shown in Fig. 2.2. FSR can be defined as

$$\Delta\lambda_{FSR} = \lambda_n - \lambda_{n+1} \tag{2.9}.$$

Using Eq. 2.2 and approximating $n \approx n+1$ for large mode orders n, the FSR can be find as

$$\Delta\lambda_{FSR} = \frac{2md}{n} - \frac{2md}{n+1} = \frac{2md}{n(n+1)} \cong \frac{2md}{n^2} = \frac{\lambda^2}{2md} \tag{2.10}.$$

In terms of frequency, the free spectral range (FSR) can be written by using c= λν in Eq. 2.10.

$$\Delta\upsilon_{FSR} = \frac{c}{\lambda^2}\Delta\lambda_{FSR} = \frac{c}{2md} \tag{2.11}$$

Using the approximation $n \approx n+1$, states that the approximation in Eq. 2.10 and Eq. 2.11 become better as n gets larger. The FSR decreases with increasing distance between the plates and with increasing refractive index of the medium inside the resonator. The spectra shown in Fig. 2.3 is calculated for a ruby slab. It can be observed that the FSR value is increasing with increasing wavelength.

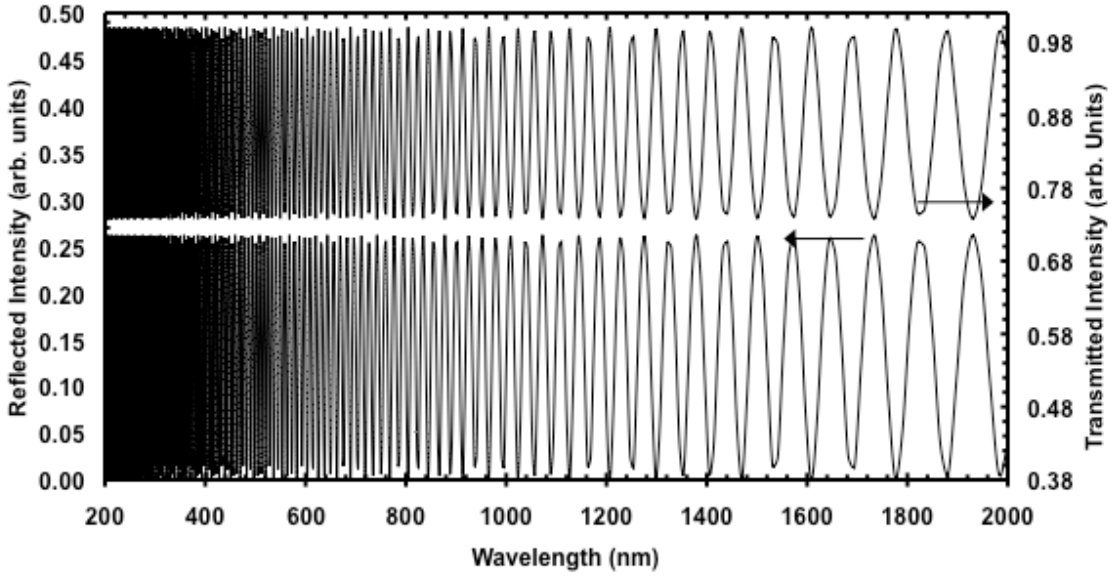

Figure 2.3. The transmitted and reflected intensities from a ruby slab with a refractive index of m=1.76 and thickness of a=500μm.

Fig. 2.3 shows that, we observe a dip in transmitted intensity, when the reflected intensity is maximum and vice versa. Moreover, the FSR value increases with the increasing wavelength. The analysis of Fabry-Perot resonator is important in understanding the general characteristics of optical resonators.

The ratio of the FSR to the linewidth of the resonance is called *finesse* (F), which is given by

$$F = \frac{\Delta\lambda_{FSR}}{\Delta\lambda_{1/2}} = \frac{\Delta\upsilon_{FSR}}{\Delta\upsilon_{1/2}} \tag{2.12}.$$

Finesse for a Fabry-Perot resonator can also be calculated using Eq. 2.13.

$$F = \frac{\pi\sqrt{R}}{1-R} \tag{2.13},$$

where R is the reflectance of the mirrors. Using the Eq. 2.12 in Eq. 2.7, we get the relation between the *Q-factor* and the *finesse*. Later if we substitute Eq. 2.10 and 2.13 into the new relation we get Eq. 2.14. Then using the relation for size parameter in Eq. 2.3 we can simplify Eq. 2.14 to

$$Q = \frac{\lambda}{\Delta\lambda_{FSR}} F = nF = \frac{2md\pi\sqrt{R}}{\lambda(1-R)} = \frac{mx\pi\sqrt{R}}{1-R} \tag{2.14}.$$

Eq. 2.14 states that; increasing refractive index, size parameter or the reflectance of the mirrors will result in higher *Q-factor* values. Moreover, the relation between *Q-factor* and the *finesse* states that; higher order modes leads to high *Q-factor* resonances. In Fig. 2.3 we can see that the quality factor is decreasing with the increasing wavelength as we expect from Eq. 2.14.

2.2.2 Phase and Intensity of Resonances

The constructive interference of multiple beams in a Fabry-Perot resonator form a resonance. The superposition of these infinite number of waves are separated by equal phase delays δ. Phase delay is due to the difference in optical path length between the transmitted waves forming a resonance. The difference in optical path length between adjacent waves with normal incidence on the plates is given by

$$\delta = (2md)k_o = mx\lambda k_o = mx2\pi \tag{2.15}$$

where k_0 is the wavenumber of the incident beam. The amplitude of the transmitted field is the sum of the amplitudes of all the transmitted components.

At each reflection from the mirrors, there will be a coefficient of r for reflection amplitude. If we denote the total transmitted field by E_t and the incident wave by $E_0e^{i\omega t}$, we can write the total transmitted field as [22].

$$\begin{aligned} E_t &= E_{1t} + E_{2t} + E_{3t} + \ldots + E_{Nt} \\ &= E_0 t^2 e^{i\omega t} + E_0 t^2 r^2 e^{i(\omega t - \delta)} + E_0 t^2 r^4 e^{i(\omega t - 2\delta)} + \ldots + E_0 t^2 r^{2(N-1)} e^{i[\omega t - (N-1)\delta]} \\ &= E_0 T e^{i\omega t}\left[1 + \mathrm{Re}^{-i\delta} + R^2 e^{-i2\delta} + \ldots + R^{(N-1)} e^{-i(N-1)\delta}\right] \end{aligned} \tag{2.16}$$

where r is the reflection and t is the transmission coefficients of the resonator surfaces. The transmittance (T) and reflectance (R) can be found by taking the square of transmission and reflection coefficients respectively. If there is no absorption, then the total transmitted and reflected intensities add up to unity. For an infinite number of waves the transmitted field is given by

$$E_t = E_0 e^{i\omega t}\left[\frac{T}{1-\mathrm{Re}^{i\delta}}\right] \tag{2.17}.$$

The difference between resonances corresponds to a phase difference of 2π. The electrical field can be written as in Eq. 2.18 including the phase φ.

$$E = E_0 e^{i(\omega t+\varphi)} \tag{2.18}.$$

If we compare Eq. 2.17 and 2.18, we can write the exponential term for $e^{i\varphi}$ as

$$e^{i\varphi} = \left[\frac{T}{1-\mathrm{Re}^{i\delta}}\right] \tag{2.19}.$$

We can rewrite the Eq. 2.19 as

$$\tan\varphi = \mathrm{Im}\left[\frac{T}{1-\mathrm{Re}^{i\delta}}\right] \Big/ \mathrm{Re}\left[\frac{T}{1-\mathrm{Re}^{i\delta}}\right] \tag{2.20}.$$

By taking the inverse of Eq. 2.20 the phase factor of the transmitted field can be written as

$$\varphi = \tan^{-1}\left(\frac{\sin\delta}{1/R-\cos\delta}\right) \tag{2.21}.$$

The output intensity is determined by the reflectance from the first interface and the incident beam intensity to the resonator. Only a fraction of light will enter the resonator

due to the reflection on the first mirror. If we denote the amount of incident light intensity to the resonator by I_0, which is 1-R, and the transmitted light intensity by I_t, the relation between them can be written as

$$\frac{I_t}{I_0} = \frac{1}{1 + \frac{4R}{(1-R)^2}\sin^2(\delta/2)} \tag{2.23}$$

From Eq. 2.23 we can interpret that the transmitted intensity is maximum when the phase change is a multiple of 2π. When the phase change is a multiple of 2π, the sinus function goes to zero as a result the transmitted intensity value takes its maximum value.

$$R + T = 1 \tag{2.24}$$

Moreover, we can calculate the reflected light intensity by substituting Eq. 2.23 into Eq. 2.24.

$$\frac{I_R}{I_0} = \frac{I_0 - I_t}{I_0} = \frac{2R(1-\cos\delta)}{(1+R^2)+2R\cos\delta} \tag{2.25}$$

2.3 Microsphere Resonator

The morphology dependent resonances (MDR'S) of a spherical object was first investigated by Gustav Mie in the beginning of 19th century [23]. In investigating the light scattering from spherical particles, the resonant circulation of optical field inside the microsphere caused the spectrum to give sharp responses. These optical modes are confined by total internal reflection (TIR) at the dielectric air interface and are often referred to as whispering gallery modes (WGM's). WGM's are originated from the

phenomenon of acoustic waves observed propagating in the interior surface of the Saint Paul's Cathedral in London, observed and published by Lord Rayleigh [23].

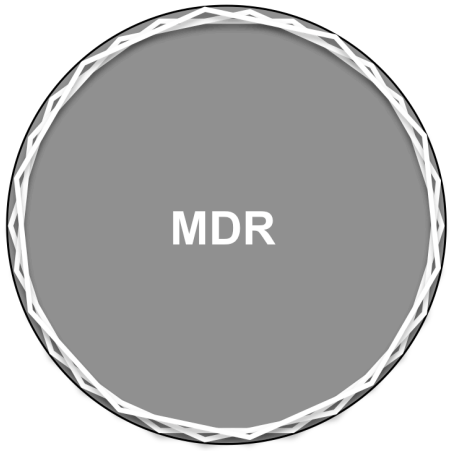

Figure 2.4: Geometrical representation of the MDR's of a spherical optical resonator.

The propagation of rays around the inner surface the microsphere, confined by an almost total internal reflection can be interpreted as the MDR's of the microsphere [24]. Only at particular wavelengths, which satisfy the MDR condition, the microsphere acts as an optical cavity. At an MDR, the light wave circumnavigating the microsphere proceeds to its initial point in phase and interferes with itself constructively. This positive interference can take place only at definite distinct MDR wavelengths [25]. Moreover, an MDR is specified by a mode order *l,* which accounts for the number of nodes in the internal intensity distribution in the radial direction, and mode number *n* indicating the number of nodes in the internal intensity distribution as the polar angle is varied from 0^0 to 180^0 [26]. Additionally, for each set of mode number and mode order, there is a transverse electric (TE) and a transverse magnetic (TM) MDR. As an optical resonator, the microsphere has its similarities with the Fabry-Perot resonator. Instead of two times the optical path (2d), the cavity is determined by the circumference of the microsphere ($2\pi a$).

Numerically, using the similar expression to the Fabry-Perot resonator in Eq. 2.2 and replacing 2d by 2πa we obtain

$$n\lambda \approx m2\pi a \tag{2.26},$$

where a is the radius of the sphere and m the refractive index of the sphere. Again the size parameter can be written as in Eq. 2.27.

$$x = \frac{2\pi a}{\lambda} \tag{2.27}.$$

Eq. 2.26 can be simplified by using the size parameter we defined.

$$n = mx \tag{2.28}.$$

The ray optic definition fails to explain the internal intensity distribution in radial direction and the polarization dependence of the resonances. Moreover, the excitation of MDR's and escape behavior of the light from the microsphere cannot be explained using ray optics. Instead, using Lorenz-Mie theory, we can explain those phenomenan. In the next section Lorenz-Mie theory is explained.

2.3.1 Lorenz-Mie Theory

A complete description of the interaction of light with a dielectric is given by the electromagnetic theory. The interaction of light with small particles (smaller than the wavelength of the light) is explained with Rayleigh scattering. The interaction of light with

bigger particles than the wavelength of the light can be explained by using Lorenz-Mie theory. In Lorenz-Mie theory, the light waves are expressed as the superposition of the electromagnetic waves. Using the appropriate boundary conditions the characteristic equations for the MDR's can be derived.

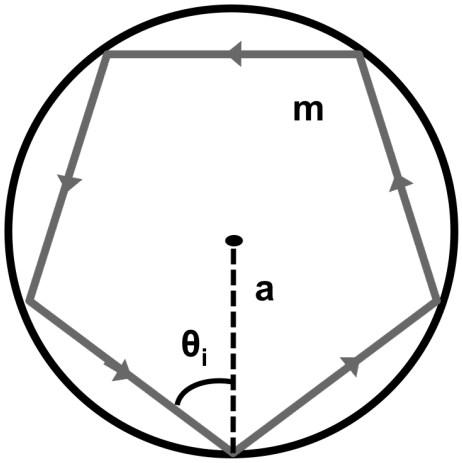

Figure 2.5 The illustration of one of the possible resonance paths inside the microsphere.

Characteristic equations for the MDR's are derived by requiring continuity of the tangential components of both the electric and magnetic fields at the boundary of the dielectric sphere and the surrounding medium. Internal intensity distributions are determined by expanding the incident wave (plane-wave or focused beam), internal field, and external field, all in terms of vector spherical harmonics and again imposing appropriate boundary conditions. This positive interference can take place only at definite distinct MDR wavelengths [25]. As in the spherical harmonics, an MDR is specified by a mode order *l,* which accounts for the number of nodes in the internal intensity distribution in the radial direction, and mode number *n* indicating the number of nodes in the internal intensity distribution as the polar angle is varied from 0^0 to 180^0 [26].

Additionally, for each set of mode number and mode order, there is a transverse electric (TE) and a transverse magnetic (TM) MDR. For optical modes having TE polarization, the characteristic equation is

$$\frac{\left[mj_n(mx)\right]'}{m^2 j_n(mx)} = \frac{\left[xh_n^{(1)}(x)\right]'}{h_n^{(1)}(x)} \tag{2.29}$$

Whereas, the characteristic equation for TM modes is given by

$$\frac{\left[mxj_n(mx)\right]'}{j_n(mx)} = \frac{\left[xh_n^{(1)}(x)\right]'}{h_n^{(1)}(x)} \tag{2.30}$$

where for both Eq. 2.29 and Eq. 2.30 the $j_n(x)$ and $h_n^{(1)}(x)$ are the spherical Bessel and the Hankel functions of the first kind, respectively. The prime in the equation denotes the differentiation with respect to the argument.

The elastically scattered field can be written as an expansion of vector spherical wave functions. The TE coefficients are denoted by b_n and TM coefficients are denoted by a_n for a plane wave. The expansion coefficients for the scattered TE field are given in Eq. 2.31.

$$b_n = \frac{j_n(x)\left[mxj_n(mx)\right]' - j_n(mx)\left[xj_n(x)\right]'}{h_n^{(2)}(x)\left[mxj_n(mx)\right]' - j_n(mx)\left[xh_n^{(2)}(x)\right]'} \tag{2.31}.$$

The coefficients for TM field are given in Eq. 2.32.

$$a_n = \frac{j_n(x)\left[mxj_n(mx)\right]' - m^2 j_n(mx)\left[xj_n(x)\right]'}{h_n^{(2)}(x)\left[mxj_n(mx)\right]' - m^2 j_n(mx)\left[xh_n^{(2)}(x)\right]'} \quad (2.32),$$

where j_n is the spherical Bessel function, and $h_n^{(2)}$ the spherical Henkel function of the second kind [27].

For a complex frequency, related to a complex size parameter, the coefficients a_n and b_n become infinite. The expansion coefficients of the internal fields of the TM (c_n) and TE (d_n) modes have the same denominators as a_n and b_n, respectively. The zeros of denominators of a_n (c_n) for the TM and b_n (d_n) for the TE modes of an MDR labeled by *n* and *l*, quantize the polar angle and radial directions [28]. The MDR's of the microsphere occur, when the denominators of Eq. 2.31 and 2.32 are zero.

2.3.2 Quality Factor

The quality factor (*Q-factor)* of a resonator gives information about the sensitivity and the resolving power of a resonator. Moreover, the performance of a resonator can be determined by the *Q-factor,* defined by Eq. 2.6.

Eq. 2.6 imposes that *Q-factor* of an optical resonator determines how long a photon can be stored inside an MDR [29]. Therefore the Q-factor of a resonance is determined by the losses. The losses are mainly due to the absorption of the sphere (Q_{abs}), the loss due to the diffraction leakage (Q_r), the loss caused by the scattering (Q_s), and the loss due to coupling ($Q_{coupling}$). The resultant Q-factor is the sum of the inverse of all *Q-factors* associated with each type of loss and given by

$$\frac{1}{Q} = \frac{1}{Q_{abs}} + \frac{1}{Q_r} + \frac{1}{Q_s} + \frac{1}{Q_{coupling}} \quad (2.33).$$

Q-factor is also defined as Q = ωτ, where ω is the optical angular frequency and τ the radiation lifetime in the microsphere [30]. For frequencies near an MDR, the electric field inside the microsphere is given by Eq. 2.34.

$$E(t) = E_0 \exp(-i\omega_0 t - \frac{\omega_o}{2Q} t) \tag{2.34}$$

If we multiply Eq. 2.34 with its complex conjugate, then we can approximate the intensity of the field (Eq. 2.35).

$$\left|E(\omega)\right|^2 \propto \frac{1}{(\omega - \omega_0)^2 + (\omega_0 / 2Q)^2} \tag{2.35}$$

The high *Q-factors* are more sensitive than the low *Q-factors* to size and refractive index changes. Very small perturbations in refractive index or size changes can be used for modulation applications.

2.3.3 Mode Spacing of MDR's

The MDR condition is satisfied at definite discrete wavelengths. The mode spacing (Δλ), is defined as the wavelength difference between two consecutive mode numbers (n) in the same mode order (l). In Fig. 2.6 the mode spacing between two consecutive resonances is shown. The mode spacing can be approximated by Eq. 2.36.

$$\Delta\lambda_{n,l} \equiv \lambda_{n+1,l} - \lambda_{n,l} \tag{2.36}.$$

The exact value of mode spacing is given Eq. 2.37. We can observe that Eq. 2.37 is very similar to Eq. 2.10 except the refractive index.

$$\Delta\lambda = \frac{\lambda^2}{2\pi a}\frac{\tan^{-1}(\sqrt{m^2-1})}{\sqrt{m^2-1}} \tag{2.37}$$

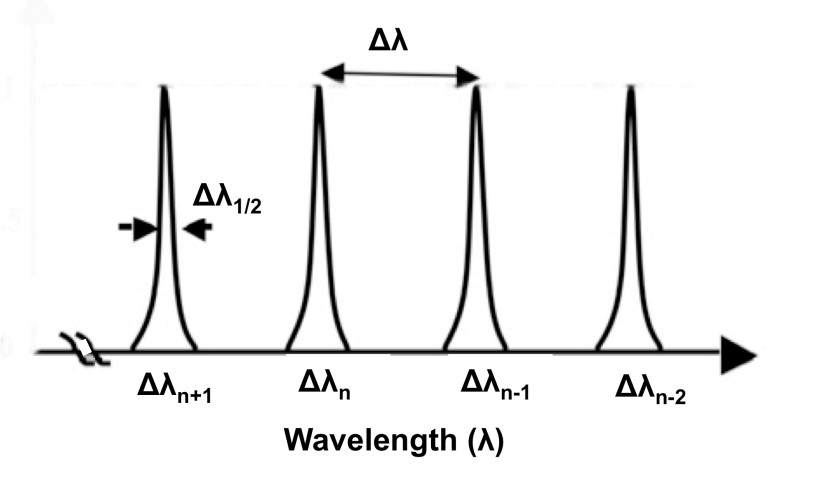

Figure 2.6 The MDR's and mode spacing Δλ between consecutive modes.

Introducing a new parameter m_{eff} (Eq. 2.38) defined as the effective index of refraction of a spherical resonator, will let us to write the equation for mode spacing as in Eq. 2.39.

$$m_{eff} = \frac{\sqrt{m^2-1}}{\tan^{-1}(\sqrt{m^2-1})} \tag{2.38}$$

$$\Delta\lambda = \frac{\lambda^2}{2\pi a m_{eff}} \tag{2.39}$$

In general, a resonator with high *Q-factor* and *finesse* is desired for communication applications.

2.4 Coupling light into MDR's of Microspheres

Coupling light into MDR's of a microsphere is a main challenge. The MDR's of a microsphere can be excited by using plane-wave or Gaussian beam illumination. In plane wave illumination, the intensity of the incoming beam is uniformly distributed. On the other hand, couplers are also used in order to couple the light into MDR's of the microsphere. There are a variety of evanescent field techniques for efficiently to coupling to MDR's of microspheres [24].

The efficiency of a coupler is determined by the overlap of the sphere and the coupler mode fields and the matching mode propagation constants. Moreover, the length of the coupler, and how steep the fiber is curled inside the coupler, play important roles in the efficiency of the evanescent coupler [31]. The excitation by an optical fiber coupler can be approximated with a Gaussian beam excitation.

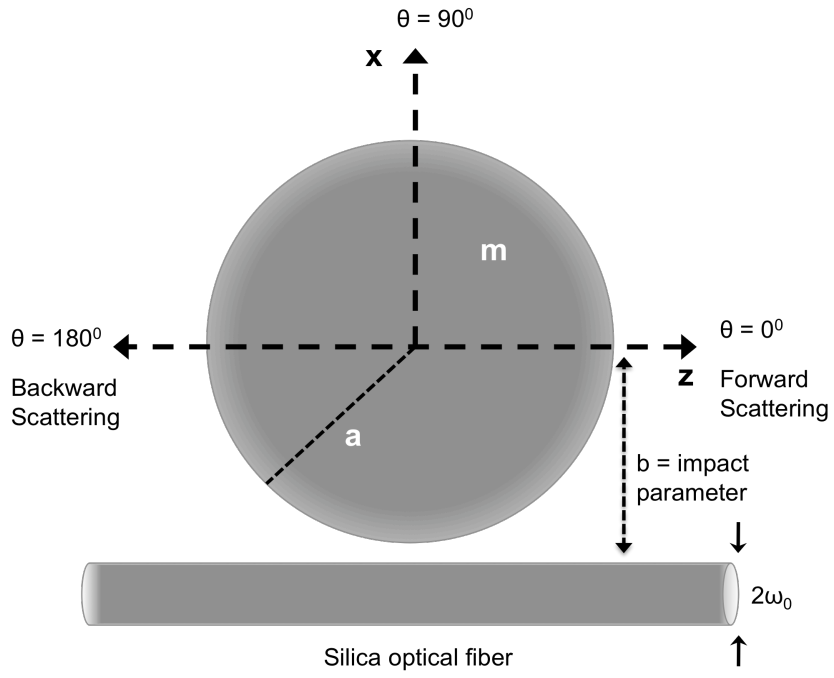

Figure 2.7 Excitation of MDR's by a Gaussian beam illumination geometry.

In a Gaussian beam excitation, the efficiency of the excitation of MDR's depend on the beam's focusing and the distance between the beam waist and the microsphere. Fig. 2.7 shows the excitation of MDR's by a Gaussian beam illumination. The distance between the beam waist and the microsphere is called the impact parameter, denoted by b. Using the localization condition the impact parameter is found to be between

$$a < b < ma \tag{2.40},$$

where a is the radius of the sphere and m the refractive index of the sphere.

2.5 Optical Fiber Half Coupler

An optical fiber half coupler (OFHC) consists of an optical fiber polished very close (couple μm) to the core and buried in the glass block. Placing a microsphere on the exposed surface near the evanescent field of the optical fiber's core will cause an energy exchange between the mode of the fiber and the MDR of the sphere. A schematic of an OFHC is shown in Fig. 2.8. The optical fiber, buried into the glass substrate to make the OFHC, is a 1500 nm single-mode fiber with a core refractive index of 1.47, and with a cladding refractive index of 1.45.

As we have discussed earlier, coupling the evanescent field of the fiber to the MDR's of the microsphere is quite challenging. Nevertheless, the OFHC also can change the results dramatically. For instance, due to the imperfections of the OFHC, the background intensity in the elastic scattering spectra can increase [31]. With a proper OFHC, which couples the evanescent field to the microsphere only at the optimal impact parameter, lower background levels can be obtained.

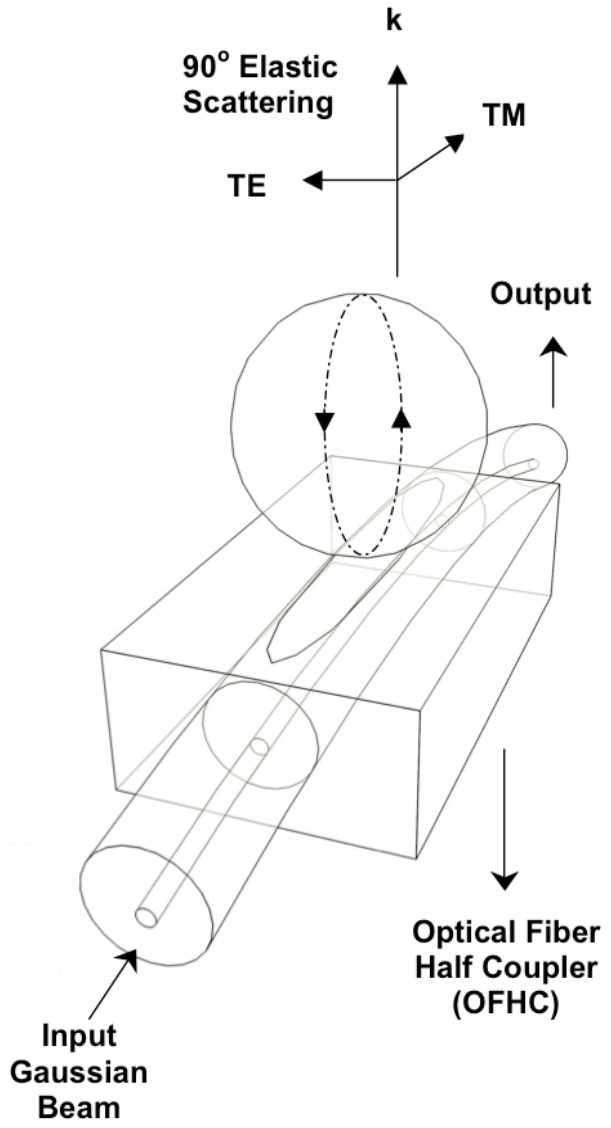

Figure 2.8 The schematic of a microsphere on the optical fiber half coupler.

Chapter 3

OPTICAL MODULATION IN SILICON

3.1 Introduction

The need for low cost photonic devices, high speed intrachip and interchip communication, and high bandwidth, low power consumption and interference free connections in conventional microelectronics, have stimulated a significant amount of research in silicon photonics [2]. Although silicon photonics, is less well developed as compared to the direct bandgap III-V semiconductor photonics technologies; silicon is poised to make a serious impact on the optical communications [32]. Integrated optoelectronic silicon chips have become a promising candidate for the upgrade of conventional microelectronics [33].

A variety of optical functionalities have already been demonstrated in silicon. The Raman gain [34], stimulated Raman scattering (SRS) [3], SRS lasing in pulse [35] modulated [36] and CW [37] silicon Raman lasers have been observed. Additionally, silicon modulators [9] have been developed first using a metal-oxide-semiconductor (MOS) capacitor [10], a Mach-Zehnder [11] configuration, SRS [12], and a microring [13] configuration, a microracetrack configuration [14], a p-i-n diode based microdisk [15], a p-n diode on a silicon waveguide [16], and a photonic crystal [17].

Researchers at Cornell University demonstrated all-optical modulators based on carrier injection effect [38]. In this work, a laser beam, which operates at a wavelength of 410 nm, is used, in order to inject free carriers. As a result of the change in the free carriers the laser beam operating at 1.5 μm is modulated.

In addition to the techniques using Kerr-effect and carrier injection effect, thermo-optical modulation has been demonstrated by Tewary et al [8]. In this work, using silicon

nanocrystal coated silica microspheres excited by a laser operating at 405nm, the light at 1.5 μm has been modulated. As a result, the pump heated the microsphere, which thermally shifted the refractive index.

Achieving modulation in silicon is quite challenging due to the non-existence of linear electrooptic (Pockels') effect due to the inversion symmetry of silicon [39]. In addition, other electrooptic effects, such as Franz-Keldysh and Kerr effects are extremely weak for silicon [39]. The most effective way of electro-optical modulation in silicon can be achieved by means of the plasma dispersion effect [40]. On the other hand, it was demonstrated that all-optical switching using bistability effect, could also used in a silicon optical modulator [41].

3.2 Electro-optical modulation

The real part of refractive index and the imaginary part of the refractive index of a material can be perturbed by applying an electric field. The change as a result of applied electric field in the real part of the refractive index is called electrorefraction and the change in the imaginary part of the refractive index due to an applied electric field is called electroabsorption. The electro-optic effects are mainly, Pockels effect, Kerr effect, Franz-Keldysh effect, and the effect of carrier injection or depletion.

3.2.1 The Pockels Effect

The Pockels effect, known as the first order electro-optic effect, causes a change in the real part of the refractive index, Δm, with the applied electric field, E. For a uniform E field and fixed modulator geometry, the change in the refractive index will be proportional to the applied voltage. According to Pockels effect, the change in the refractive index depends on the direction of the applied E field with respect to the axes of the modulator crystal. However, simplifications occur in any given crystal symmetry direction.

By aligning the applied field with one of the principal axes, the largest electro-optic coefficients can be utilized. For instance, the maximum refractive index change for lithium niobate ($LiNbO_3$) occurs, if 'r_{33}' coefficient is used. The value of r_{33} is 30.8 x 10^{-12} m/V. The refractive index change for $LiNbO_3$ is given by Eq. 3.1.

$$\Delta m = -r_{33} m_{33} \frac{E_3}{2} \qquad (3.1),$$

where m_{33} is the refractive index in the direction of the applied field, and E_3 is the applied electric field [39]. However, Pockels effect is not an optical modulation option for silicon, since the Pockels effect disappears completely for silicon.

3.2.2 The Kerr Effect

The Kerr effect, also known as the second order electro-optic effect, causes a change in the real refractive index, which is proportional to the square of the applied electric field. This effect is a relatively weak effect in silicon. The change in the real part of the refractive index with the applied electric field is given by

$$\Delta m = s_{33} m_0 \frac{E^2}{2} \qquad (3.2).$$

where s_{33} is the Kerr coefficient, m_0 the initial refractive index, and E the applied electric field. Unlike the Pockels effect, the Kerr effect is independent of the direction of the applied field.

3.2.3 The Franz-Keldysh Effect

The Franz-Keldysh effect explains the distortion of energy bands as a result of applied voltage. This effect is mainly dominant at wavelengths close to the material's bandgap. The applied electric field causes a change in both the real part and the imaginary part of the refractive index. The energy bands of the semiconductor experience a distortion due to the applied voltage, and this shifts the energy bandgap, which results in the absorption of the material particularly at wavelengths close to the bandgap.

In order to see a change in the refractive index in the order of 10^{-4}, a potential difference of 200 kV/cm has to be applied [40]. On the other hand, according to Kerr effect, in order to observe a change in the refractive index in the order of 10^{-4}, a potential difference of 1000 kV/cm has to be applied. However, the Franz-Keldysh effect diminishes significantly for silicon at telecommunication wavelengths.

3.2.4 Carrier Injection or Depletion

The change in the concentration of free charges in a semiconductor material can also cause a shift in the refractive index of the material. According to Drude-Lorenz equation, the change in the absorption coefficient of the material is related to the concentration of free carriers.

$$\Delta k = \frac{e^3 \lambda_0^2}{4\pi c^3 \varepsilon_0 n}\left(\frac{N_e}{\mu_e \left(m_{ce}^*\right)^2} + \frac{N_h}{\mu_h (m_{ch}^*)^2}\right) \tag{3.3},$$

where k is the absorption coefficient, N_e the concentration of electrons, N_h the concentration of holes, λ the vacuum wavelength, c the speed of the light in vacuum, ε the permittivity of the vacuum, δN_e the change in the number of the electrons, δN_h the change

in number of holes, μ_e the electron mobility, μ_h the hole mobility, m_{ce}^* the conductivity effective mass of electrons, and m_{ch}^* the conductivity effective mass of holes. The conductivity effective mass $m_{ce}^* = 0.26\ m_0$ and $m_{ch}^* = 0.39\ m_0$, where m_0 is the electron mass [40]. Similarly, the corresponding equation for the change in the real part of refractive index (m) is given by

$$\Delta m = \frac{-e^2\lambda_0^2}{8\pi^2 c^2 \varepsilon_0 n}\left(\frac{N_e}{m_{ce}^*} + \frac{N_h}{m_{ch}^*}\right) \tag{3.4}$$

In a detailed study about the electro-optical properties of silicon, carried out by Soref and Bennett [40], the change in the real part and the imaginary part of the refractive index at telecommunication wavelengths has been illustrated experimentally. It is found that their results are in good agreement with the classical Drude-Lorenz model for electrons. On the other hand, for holes there is an $(\Delta N)^{0.8}$ dependence. The following expressions gives the changes in the refractive index of silicon due to carrier injection or depletion at communication wavelengths.

For $\lambda = 1.55\ \mu m$,

$$\Delta m = \Delta m_e + \Delta m_h = -[8.8 \times 10^{-22}\ \Delta N_e + 8.5 \times 10^{-18}\ (\Delta N_h)^{0.8}]$$
$$\Delta k = \Delta k_e + \Delta k_h = 8.5 \times 10^{-18}\ \Delta N_e + 6.0 \times 10^{-18}\ \Delta N_h \tag{3.5}$$

For $\lambda = 1.3\ \mu m$,

$$\Delta m = \Delta m_e + \Delta m_h = -[6.2 \times 10^{-22}\ \Delta N_e + 6.0 \times 10^{-18}\ (\Delta N_h)^{0.8}]$$
$$\Delta k = \Delta k_e + \Delta k_h = 6.0 \times 10^{-18}\ \Delta N_e + 4.0 \times 10^{-18}\ \Delta N_h \tag{3.6}$$

where Δm_e is the change in the refractive index of silicon due to the change in the electron concentration, Δm_h the change in the refractive index of silicon due to the change in the hole concentration, Δk_e the change in the absorption coefficient of silicon due to the change in the electron concentration, and Δk_h the change in the absorption coefficient of silicon due to the change in the hole concentration.

If the concentration of electrons is changed by 10^{17}, the refractive index of the silicon changes in the order of 10^{-4}. As a result, we can conclude that carrier injection is larger than the other effects. Furthermore, it is possible to see higher carrier injection levels by doping the silicon. In fact, p-n [16] or p-i-n [15] junction modulators have been reported, which enable higher injection levels. It should be noted that, if the carriers are injected, the refractive index will decrease.

3.3 Thermo-optical Modulation

Optical modulation can be achieved by thermo-optic effect in addition to the electric field effects and carrier injection-depletion effects on silicon. The index of refraction of silicon is changed by applying heat on the material. However, applied thermal power increases the refractive index of the silicon, which is unlike the electric field effects and carrier injection effect. The change in the refractive index as a result of applied thermal power is given by

$$\frac{dm}{dT} = 1.86x10^{-4} / K \qquad (3.7).$$

Controlling the temperature rise and the location of heat, the low efficiency in delivering the thermal energy, and low speed modulation rates are the drawbacks of this technique. In addition, the size of the silicon also increases as a result of the thermal expansion of silicon given by Eq. 3.8.

$$\alpha = 2.62 \times 10^{-6} /K \quad (3.8).$$

In fact, the size of the silicon modulator changes by the applied thermal power, which will lead to an additional red shift of the MDR wavelength. Moreover, it should be noted that the electric field effects and the carrier injection effect is decreasing the refractive index of the silicon, whereas the refractive index increases with the applied thermal power. As a result, these effects need to be considered before modulator design.

3.4 All-optical Modulation

In addition to the other modulation techniques, optical modulation can be achieved by using another light source. In fact, direct control of the refractive index by optical intensity through the third-order nonlinearity in materials, provides direct modulation of light by another light source [42]. Light can be modulated by shining very short and very intense optical signals to semiconductors.

Chapter 4

ELECTRICAL CHARACTERIZATION OF THE SILICON MICROPHERES

4.1 Metal Semiconductor Metal Contact

In our study, golden probes are designed in order to apply a potential difference to the sphere. Fig. 4.1 shows an schematic of the holder. As seen in Fig.4.1, these holders have a curved interface in order to increase the contact area with the sphere.

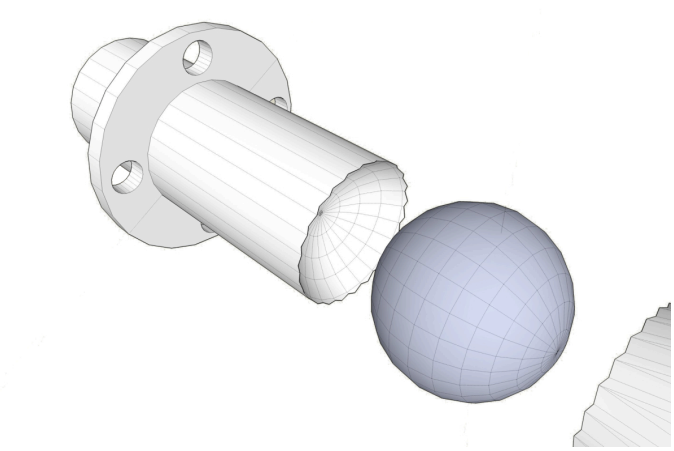

Figure 4.1 The schematic of the gold probes and the silicon microsphere.

When a metal and a semiconductor is brought into contact, the conduction and the valence bands of the semiconductor are brought into an energy relationship with the Fermi level of the metal. The type of the contact can be either Ohmic or Schottky. The designed holders consist of 60% gold and 40% percent copper. The contact type depends on the type of the metal and type of the semiconductor. The metal type and the semiconductor used in

our study is shown in Fig. 4.2. Ohmic contact and Schottky contact are explained in detail in following sections.

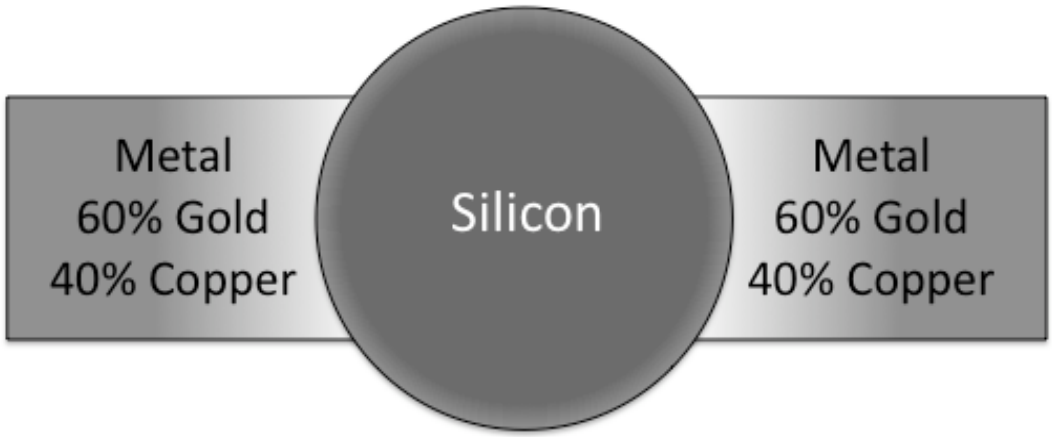

Figure 4.2 The schematic of the metal contacts and the silicon microsphere.

4.2 Schottky Junction

A metal-semiconductor junction, that does rectify current, is called a Schottky junction. The junction depends on the metal's work function, and the bandgap of the semiconductor. When a metal and a semiconductor are joined, some of the electrons in the semiconductor move into metal surface. The electrons moving to metal leave behind positively charged donors in the semiconductor. Moreover, they form a negatively charged surface on the metal. The region, where the electrons are depleted, is called the depletion region. The potential in this region is the difference between work function of metal and semiconductor. This junction behaves different in forward bias or reverse biasing. It only allows the current flow in one direction [43]. Fig. 4.3 shows the energy band diagrams of a p-type semiconductor metal junction, before and after contact. Our silicon microsphere is characterized as p-type, during the measurements.

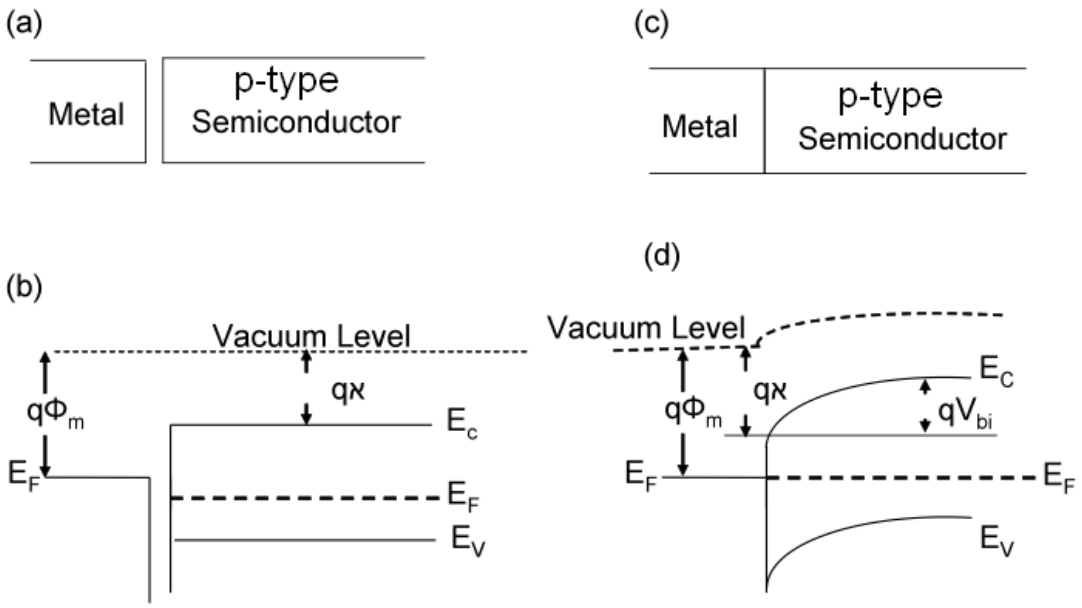

Figure 4.3 (a) One dimensional structure of a metal-semiconductor (a) before, (c) after contact, energy band diagram of a p-type semiconductor (b) before, and (d) after the contact [44].

The metal semiconductor metal (MS) structure will form a diode, and metal semiconductor (p-type) metal (MSM) structure will form two diodes connected to back to each other, as shown in Fig. 4.4.

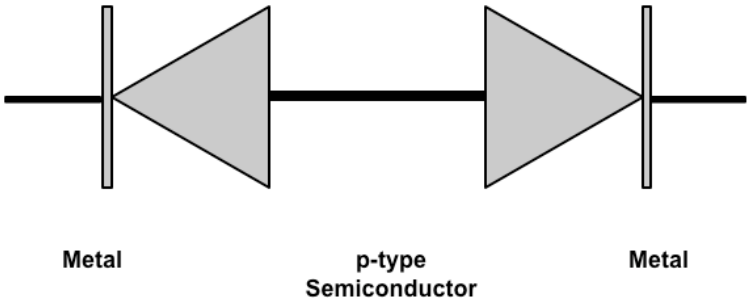

Figure 4.4 The schematic of an MSM diode.

4.4 Electrical Characterization

The silicon microsphere is placed in between two gold probes, providing the electrical input and at the same time holding the sphere. The silicon microsphere and the gold probes are shown in Fig. 4.5. The probes are made of 60% gold and 40% copper. In order to characterize the contacts and the electrical behavior of our sphere at different voltages, we built a setup as shown in Fig. 4.6. Two programmable dc power supplies are used in order to apply reverse or forward bias to the sphere.

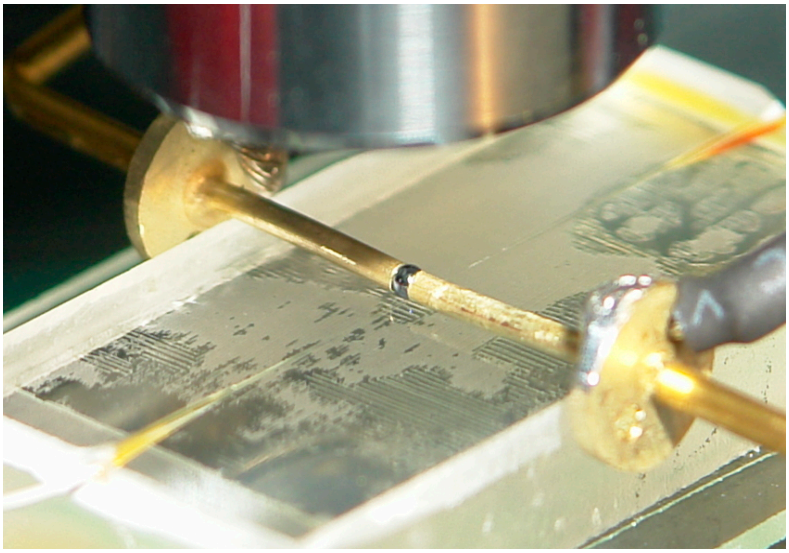

Figure 4.5 A picture of the silicon microsphere in between the two gold electrodes.

The control of dc power supplies are carried out by a computer via serial port. An oscilloscope is used to measure the voltage on the sphere. The read-out from the oscilloscope is made via GPIB protocol. Moreover, an ampermeter is used in order to measure the current passing through the circuit. Current data from the ampermeter is obtained via USB port. All the control and data-acquisition is performed using a LabView® code designed for I-V measurements.

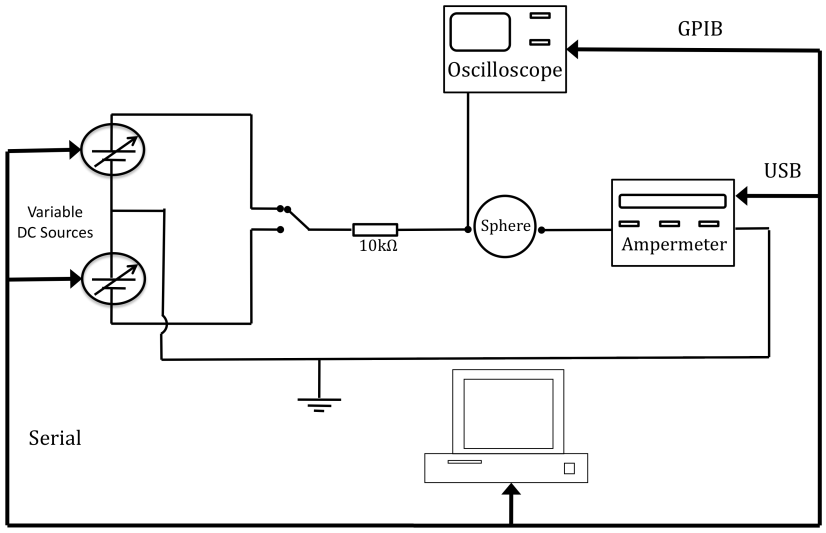

Figure 4.6 The schematic of the I-V measurement setup.

DC power supplies, ampermeter, oscilloscope and the sphere are connected to I-V measurement box, which enables easy connection between the sphere and those devices. The schematic of the box is given in Fig. 4.7. Moreover, a 10kΩ resistance is inserted in between the sphere and the voltage sources in order to prevent excess current flow. Furthermore, a switch is placed at the input of the box, which can switch the polarity. Two other switches are used in order to by-pass the resistance and the ampermeter. By the help of these two switches, the voltage from the dc source can be directly applied to sphere.

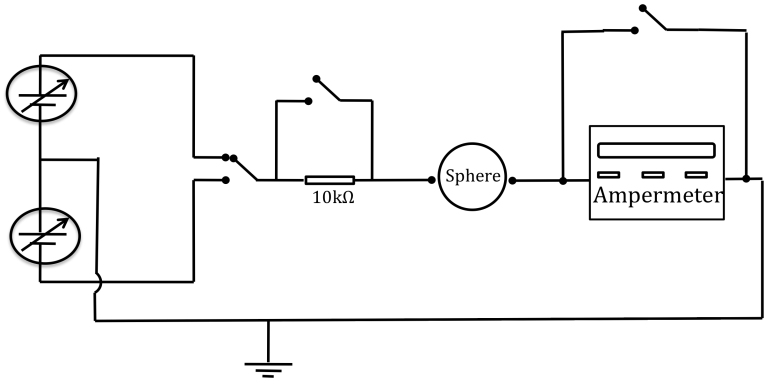

Figure 4.7 The schematic of the I-V measurement box.

In Fig. 4.8 the I-V result for the silicon microsphere is shown. 10kΩ resistance is placed in series with the sphere during the measurements. It can be observed that the device is acting like a two back to back Schottky diodes as expected. The arrow on the figure shows the transition region. We have chosen the region, shown by the arrow, for the electrical characterizations with ac signal. The modulation results are obtained in the transition region.

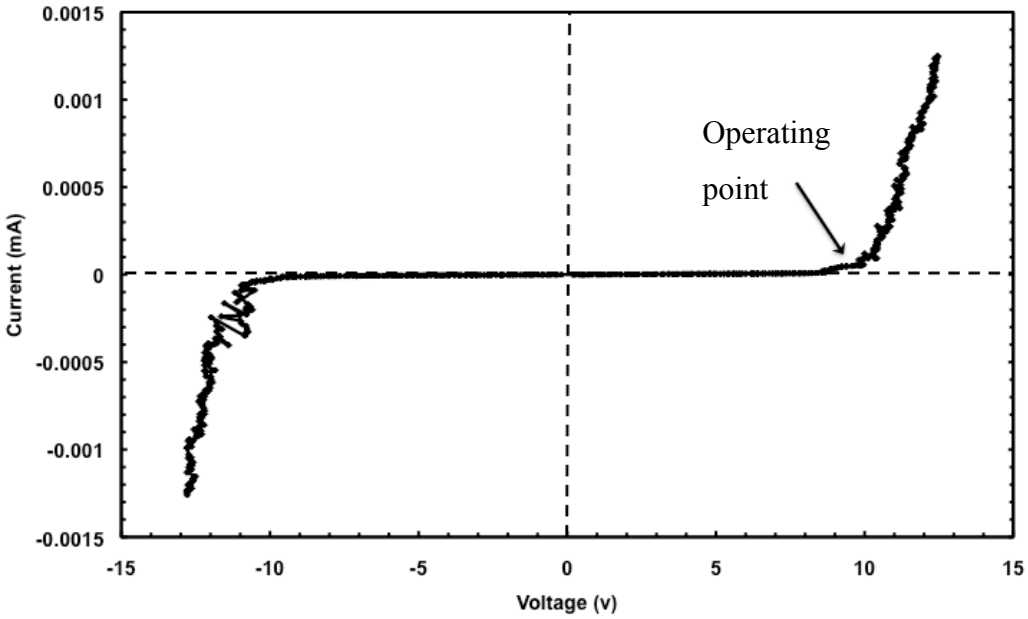

Figure 4.8 Current versus voltage response of the silicon microsphere.

In order to perform electrical characterization with an ac signal, the dc power supplies are replaced with a signal generator. Similarly, an oscilloscope is used to measure the voltage on the sphere. The ampermeter is replaced with a current amplifier. By the help of the current amplifier, the current on the sphere is monitored in real time. The output of the signal generator and the current amplifier are connected to the oscilloscope in order to capture the waveform graphs. The I-V measurement box is also used to make the necessary connections between the current amplifier, the oscilloscope, the signal generator, and the

silicon microsphere. The schematic of the setup is shown in Fig. 4.9. The data acquisition is performed by a LabView® code, which is designed to capture the data on the screen of the oscilloscope.

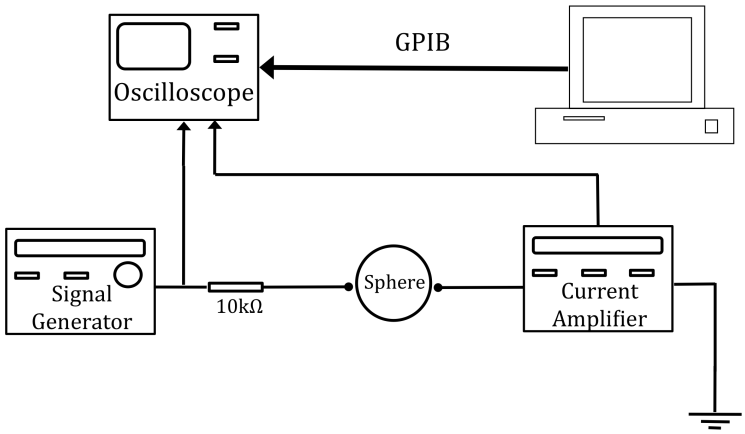

Figure 4.9 The schematic of the electrical characterization setup.

First, a sinusoidal signal is applied to the silicon microsphere oscillating between 5V and 10V. Fig. 4.10 (a) shows the applied voltage to the signal microsphere. Fig. 4.10 (b) shows the current measured on the sphere. The gain of current amplifier is adjusted 10^4 V/A which, corresponds to 0.005 mA at the maximum point. The output of the current amplifier is an inverting output, but the voltage is inverted again on the oscilloscope. The resistance of the silicon microsphere is measured to be 0.2 MΩ and capacitance 0.2 nF. Using the resistance and the capacitance the cutt-off frequency is calculated as 4kHz. Moreover, the impedance of the silicon microsphere at 10Hz is calculated using $Z^2=R^2+1/(2\pi f)^2C^2$ resulting to $80x10^6\Omega$.

In Fig. 4.10 (b) we can see that the current is cropped at the bottom part. In fact, it is not a complete sinusoidal waveform, although we apply a sinusoidal waveform. We can deduce that there is no current flow on the sphere up to certain limit. After certain potential value current flow starts on the sphere. This is also shown in Fig. 4.8. The arrow in Fig. 4.8 shows the point when the current flow starts.

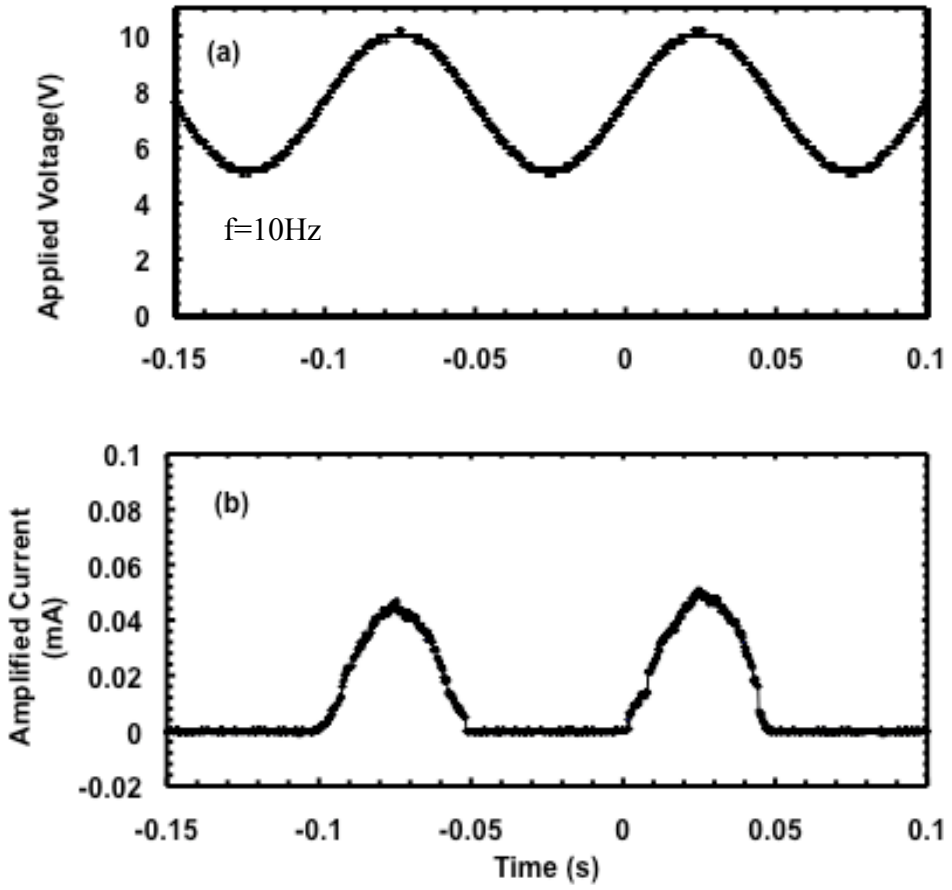

Figure 4.10 (a) Applied voltage to the silicon microsphere, and (b) the amplified current on the silicon microsphere.

Later, square waves oscillating between 0V and 10V at different duty cycles are applied to the silicon microsphere at 10Hz as shown in Fig. 4.11 and 4.13. Before the electrooptical modulation experiment, the electrical behavior of the silicon microsphere is analyzed at the same signal shapes, which were used for modulation input voltage. Fig. 4.12 and 4.14 it show that the current on the silicon microsphere follows the speed and the shape of the applied voltage.

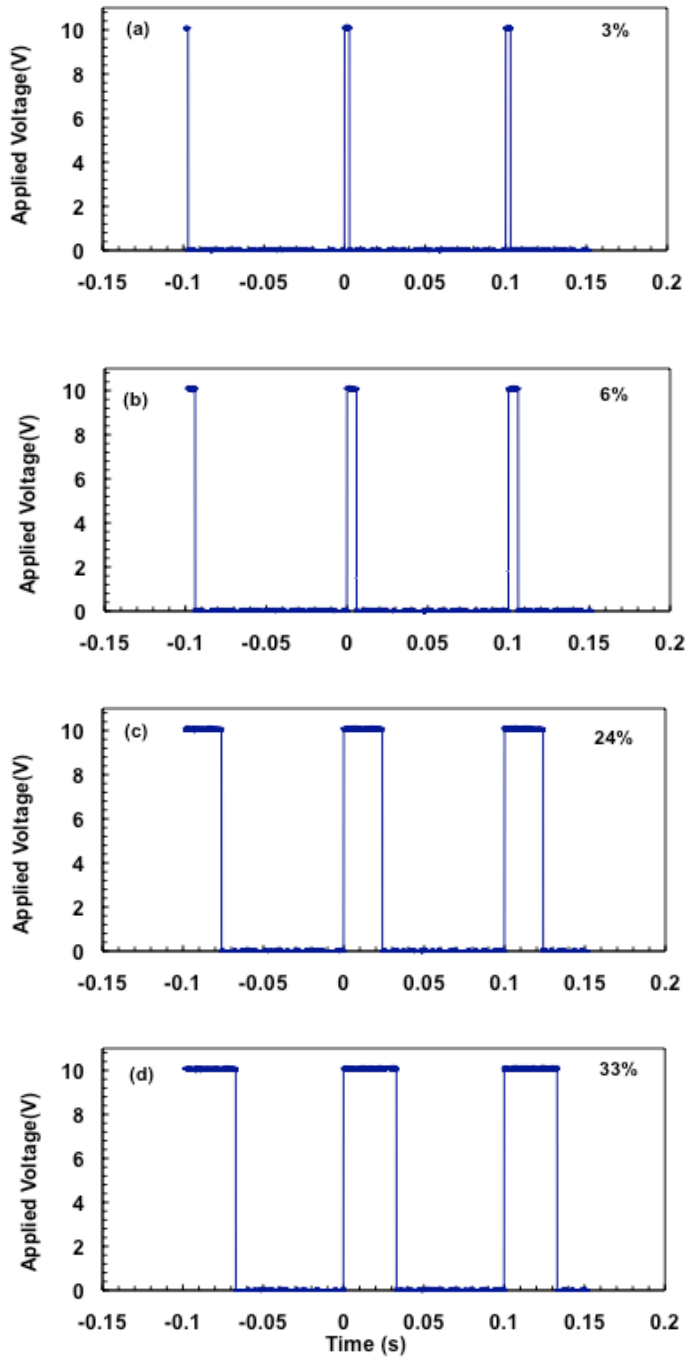

Figure 4.11 Applied voltage at (a) %3 (b) %6 (c) %24 (d) %33 duty cycle.

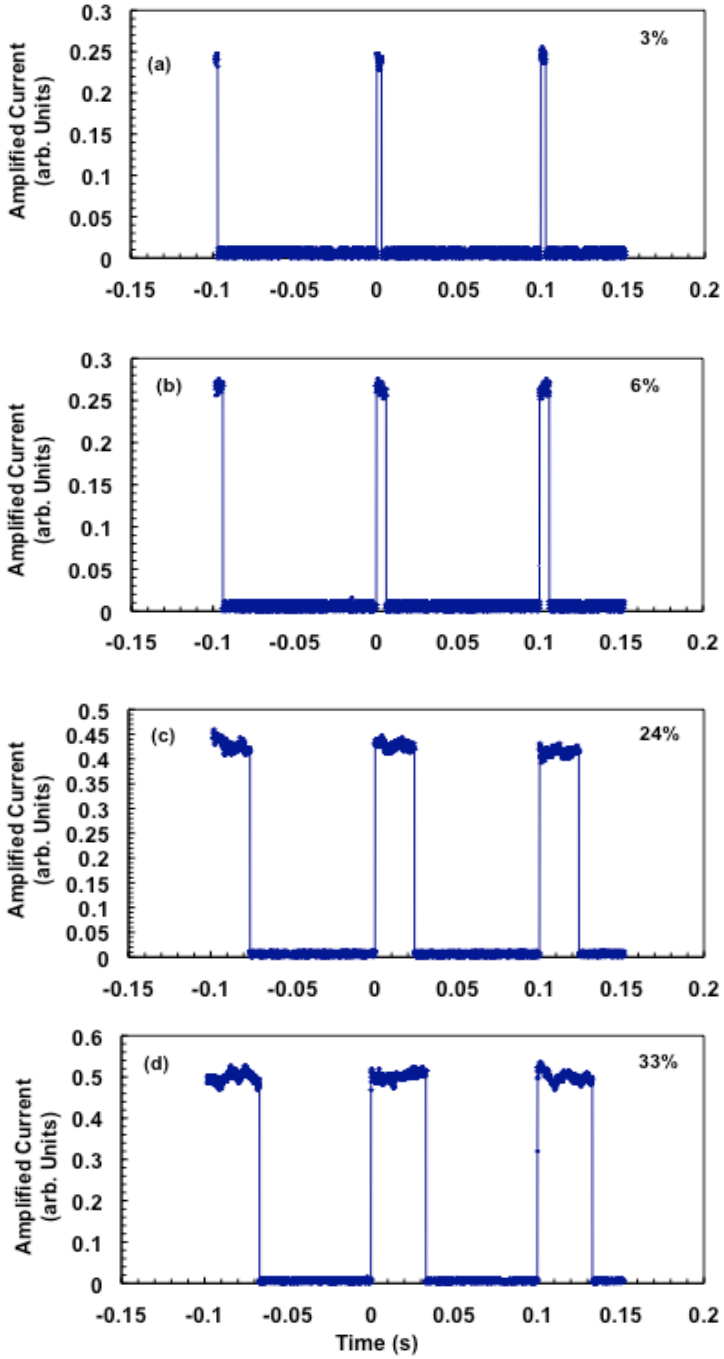

Figure 4.12 Measured current at (a) %3 (b) %6 (c) %24 (d) %33 duty cycle.

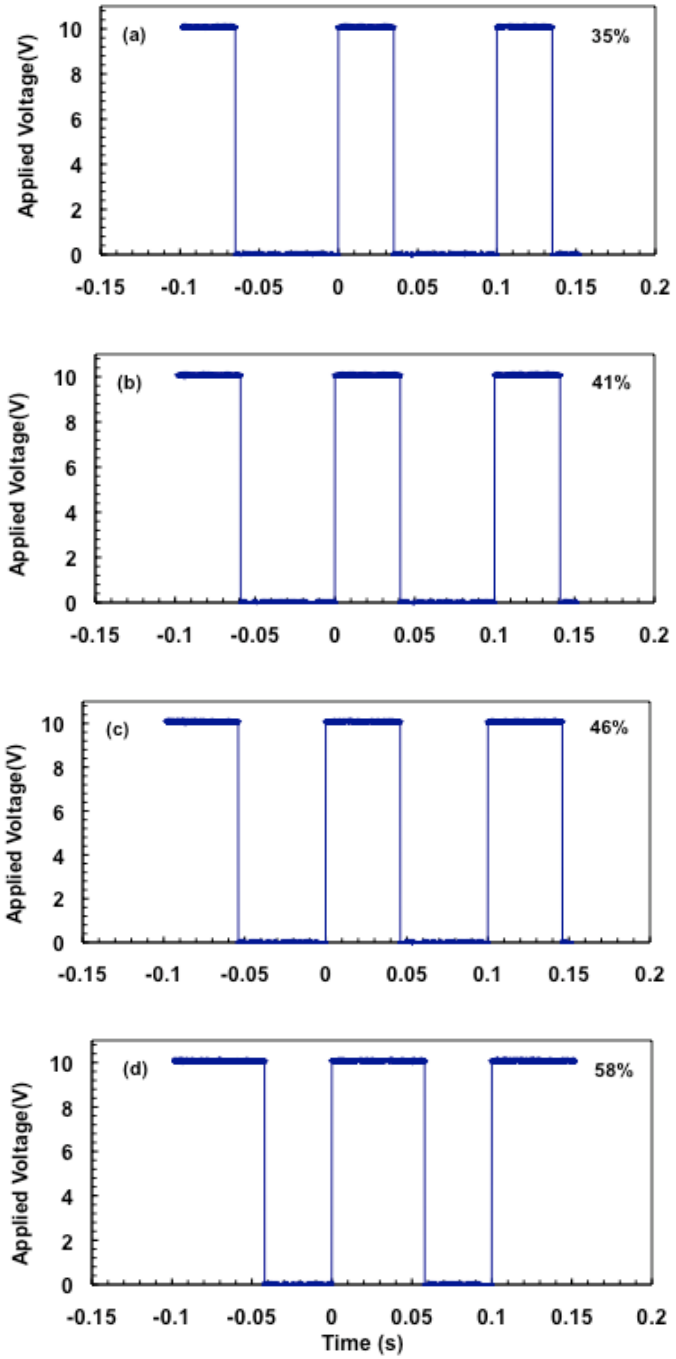

Figure 4.13 Applied voltage at (a) %35 (b) %41 (c) %46 (d) %58 duty cycle.

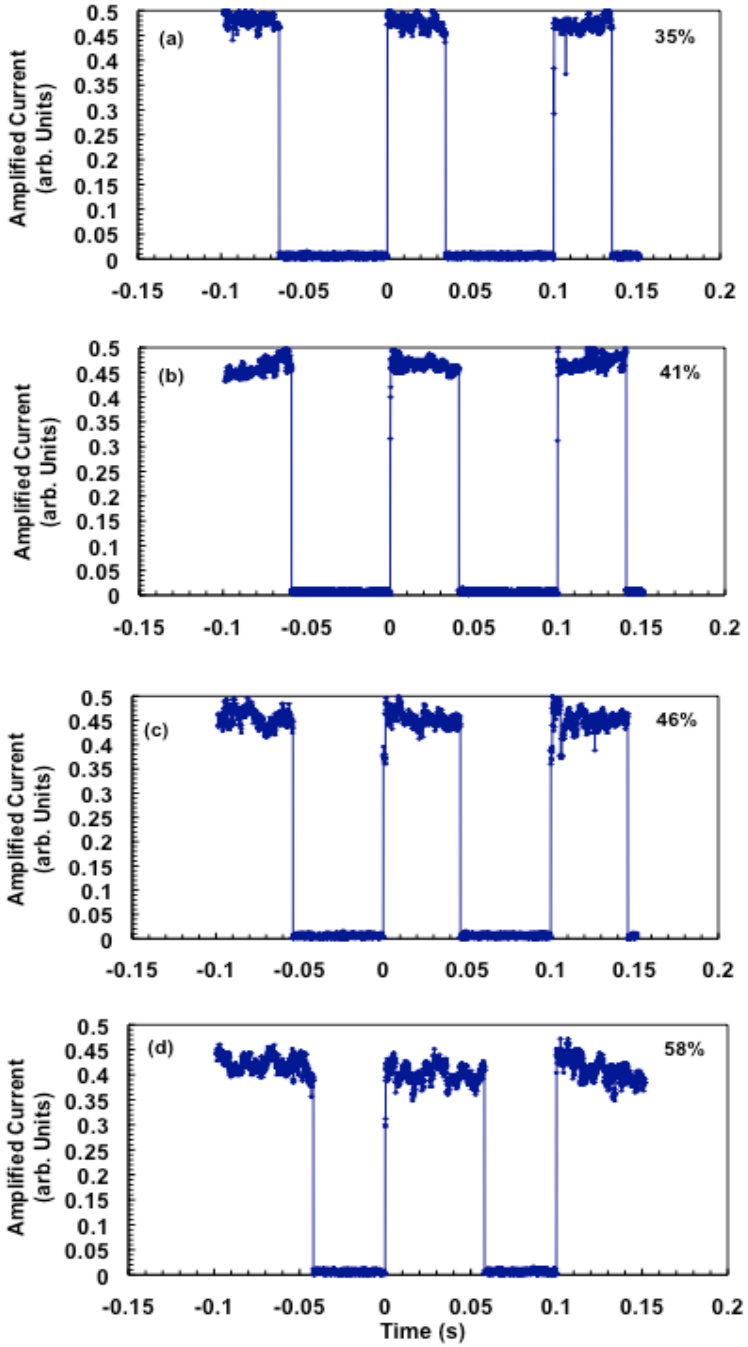

Figure 4.14 Measured at (a) %35 (b) %41 (c) %46 (d) %58 duty cycle.

Table 4.1 shows the maximum current value, maximum applied voltage and the power dissipated on the sphere at different operating duty cycles. We observed that the current on the sphere starts to oscillate as a result of increasing duty cycle, which can be observed especially in Fig. 4. 14(d).

Table 4.1 Current, impedance, and dissipated power on the sphere at different duty cycles.

Parameter	**Units**	**Values**							
Duty Cycle	**(%)**	3	6	24	33	35	41	46	58
Impedance	**(MΩ)**	0.4	0.38	0.23	0.2	0.19	0.19	0.21	0.23
Maximum Current	**(mA)**	0.025	0.026	0.042	0.050	0.052	0.051	0.047	0.043
Dissipated Power	**(μW)**	7.5	15.6	100	165	175	205	216	250

Finally, we measured the current on the sphere at slower frequencies in order to monitor the current on the sphere. Fig. 4.15 shows the applied voltage to the sphere at 0.1Hz and the measured current on the sphere at 30% duty cycle. The maximum current measured on the sphere is 0.052 mA. In Fig. 4.15 we can observe that instead of a steady current we observe an oscillating current on the silicon microsphere although the input voltage is not changing.

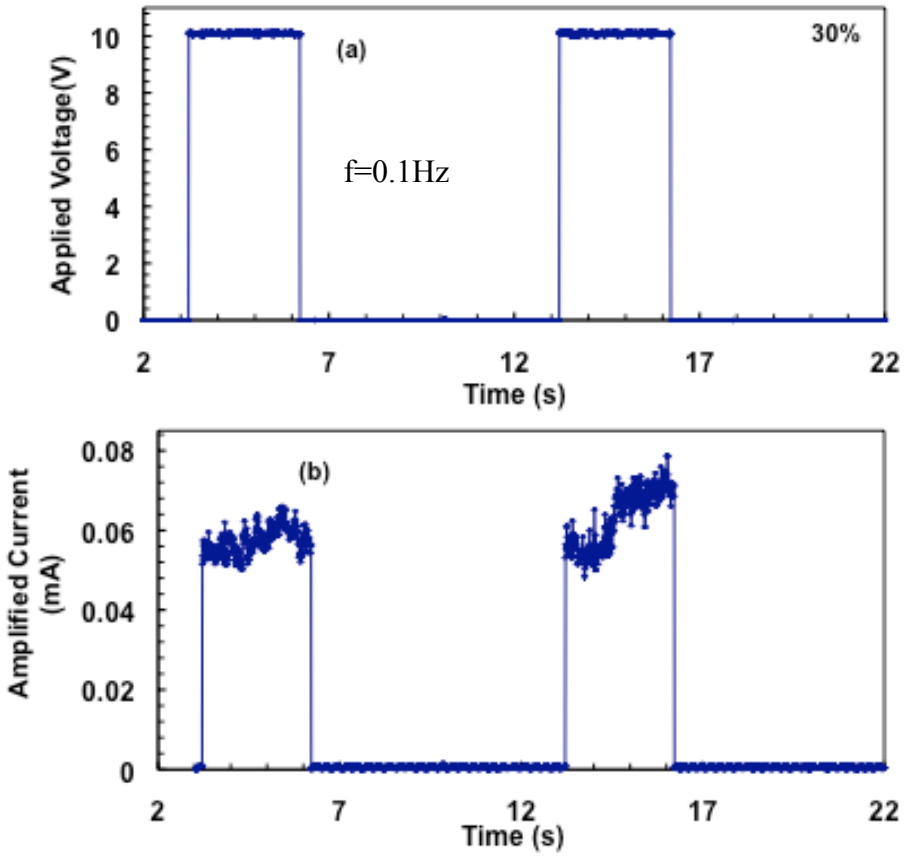

Figure 4.15 (a) Applied voltage to the silicon microsphere and (b) measured current on the silicon microsphere at %30 duty cycle.

Chapter 5

OPTICAL MODULATION AND SPECTROSCOPY

5.1 Experimental Results

In this section elastic scattering and transmission spectra, modulation results and spectroscopic result obtained by tuning of the silicon microspheres are discussed. At first a tunable distributed feed back (DFB) diode laser operating at 1473 nm is used in order to observe the MDR's of the silicon microsphere. Later, this laser is replaced with a high power diode laser operating at 1545 nm in order to perform the modulation experiment. In all the measurements a silicon microsphere with a radius of 500 μm is used.

5.1.1 Observations of MDR's from a Silicon Microsphere

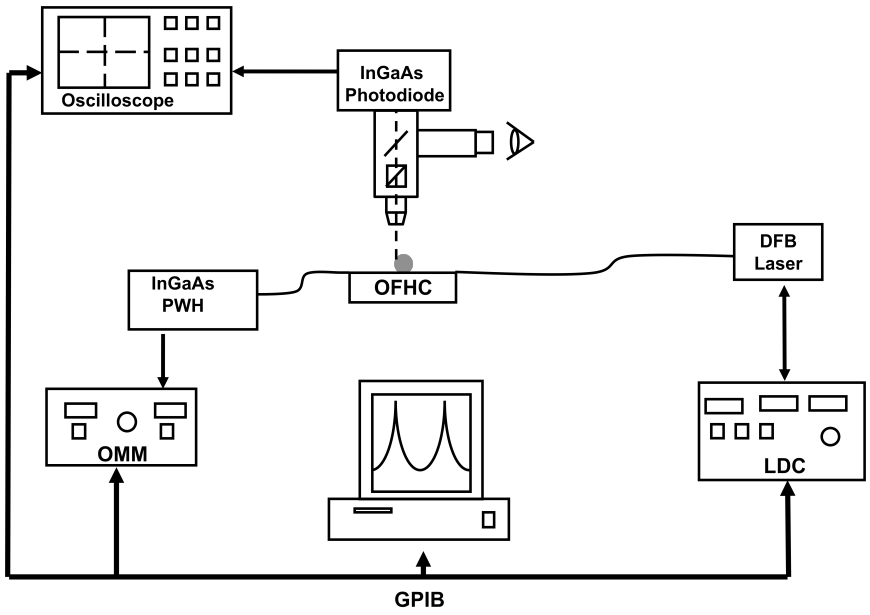

Figure 5.3 The schematic of the experimental setup.

Fig. 5.3 shows the experimental setup used to measure the transmission and scattering spectra from the silicon microsphere. A fiber coupled tunable DFB semiconductor near infrared diode laser operating in the ITU-T S-band is used to excite the microsphere MDR's. By using a laser diode controller (LDC) the wavelength of the DFB laser is tuned between 1472 nm and 1474 nm. The scattered light from the microsphere at 90^{o} is collected by a microscope lens and detected by an InGaAs photodiode (PD). The transmitted power through the optical fiber is detected by an InGaAs power wave head (PWH), which is connected to an optical multimeter (OMM). The InGaAs PD, which detects the 90^{o} elastic scattering signal, is connected to a digital oscilloscope for signal monitoring and data acquisition. The control of LDC, OMM, and the digital oscilloscope is performed using the standard IEEE-488 GPIB interface.

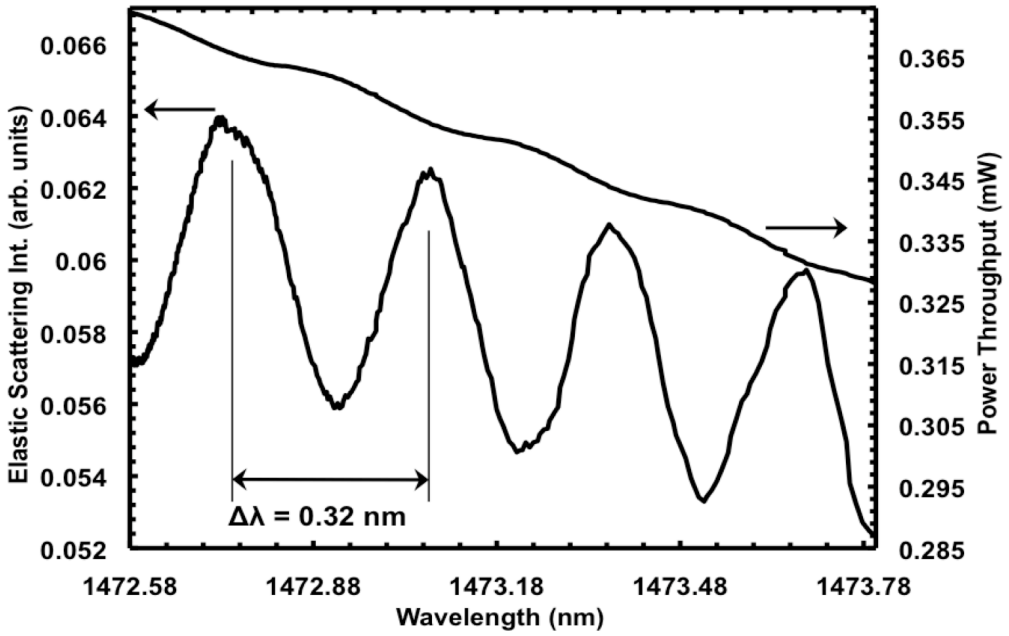

Figure 5.4 Low resolution elastic scattering and transmission spectra from a silicon microsphere with a radius of 500 μm.

Fig. 5.4 illustrates the low-resolution transmission and the 90^{o} elastic scattering spectrum from a silicon microsphere. The temperature of the DFB laser was scanned from 13 ^{o}C to 16 ^{o}C at a constant laser diode driving current of 26.3 mA. Tuning of the temperature of the LDC leads to a change in the wavelength between 1472.6 nm and 1473.8 nm. The upper curve shows the transmission spectra, whereas the lower curve shows the 90^{o} elastic scattering intensity. The mode spacing is measured to be $\Delta\lambda$ = 0.32 nm, which correlates well with the size and refractive index of the silicon microsphere.

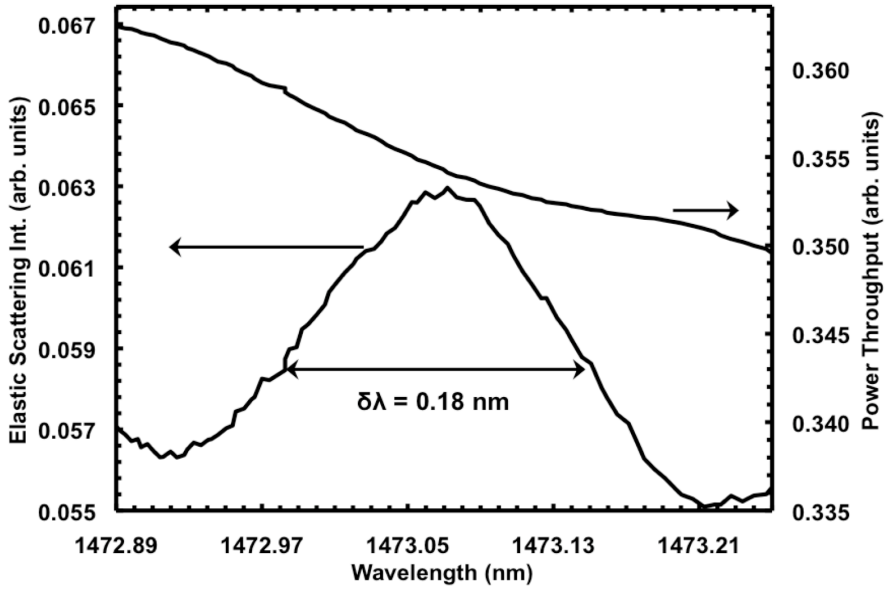

Figure 5.5 High-resolution elastic scattering and transmission spectra from a silicon microsphere with a radius of 500 μm.

Fig. 5.5 shows the high-resolution transmission (upper curve) and 90^{o} elastic scattering lower curve) spectra from the silicon microsphere. The linewidth of the MDR at 1473.06 nm is measured to be $\delta\lambda$ = 0.18 nm, leading to a quality factor on the order of 10^4, and a mode finesse of approximately 2.

5.3.2 Optical Modulation with Silicon Microspheres

In order to demonstrate optical modulation using a silicon microsphere, first we use a tunable DFB laser. The wavelength of the diode laser has been adjusted to a MDR at 1472.79 nm by setting the diode laser temperature to 13.6 ^{o}C. A laser diode controller (LDC) has been used in order to control the temperature and the current of the diode laser.

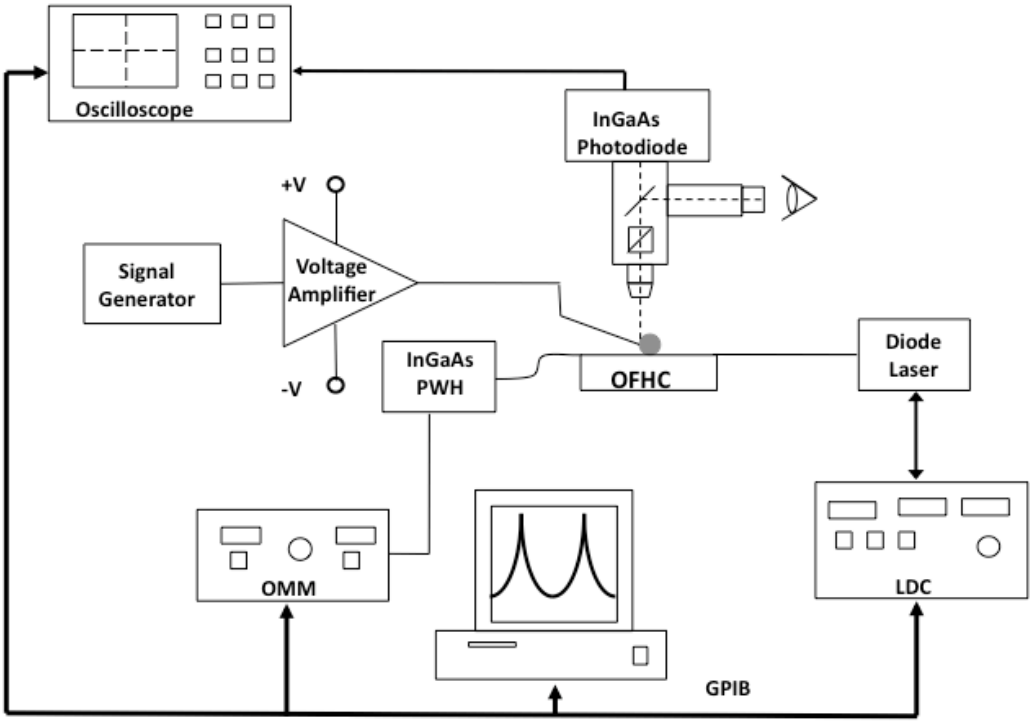

Figure 5.6 The schematic of the experimental setup.

As shown in Fig. 5.6, the power and the transmitted light through the optical fiber is detected by an InGaAs power wave head (PWH) and monitored by an optical multimeter (OMM). The elastically scattered light from the microsphere at 90^{o} is collected by a microscope lens and, through a Glan polarizer, is detected by an InGaAs photodiode (PD). The elastic scattering signal from the PD, and the input signal were all fed to a digital storage oscilloscope for signal monitoring and data acquisition.

In order to supply the modulation, a signal generator is used to generate a square wave. The square wave generated by the signal generator is fed into an amplifier in order apply higher voltages. The amplifier is fed with two dc supplies. The schematic of the amplifier circuit is shown in Fig. 5.7.

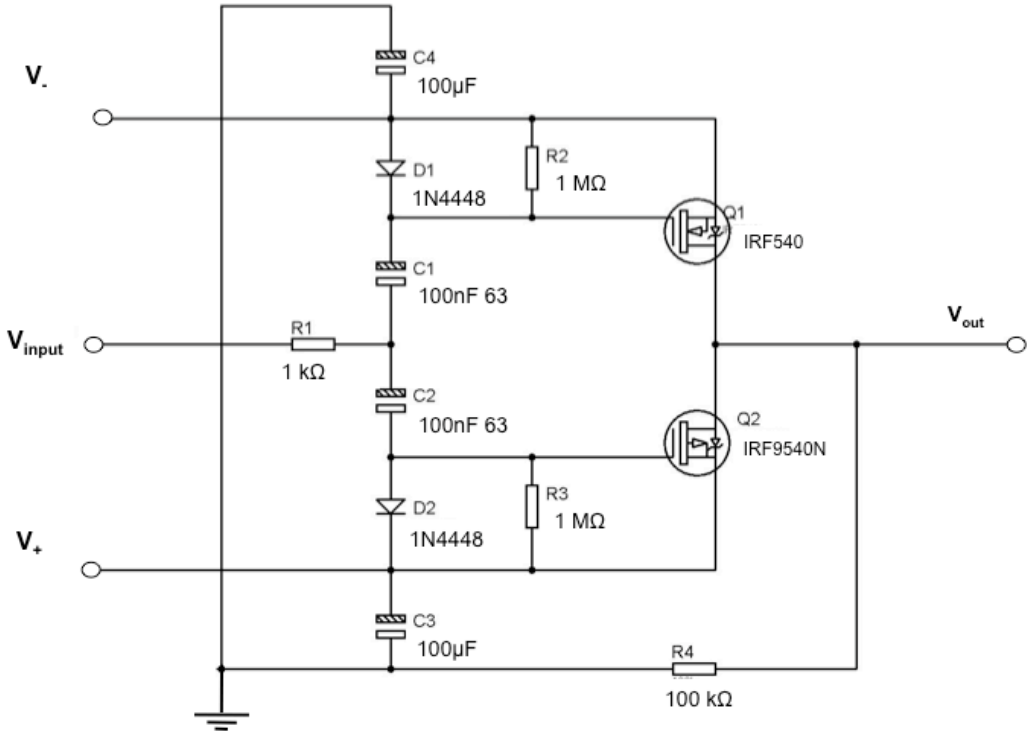

Figure 5.7 The schematic of the ac amplifier circuit.

Using the setup shown in Fig. 5.6 the modulated transmitted signal and the TE polarized elastic scattering has been obtained. The applied voltage to the silicon microsphere is shown in Fig. 5.8 (a). TE polarized elastic scattering is shown in Fig. 5.8 (b), whereas Fig. 5.8 (c) shows the transmitted signal.

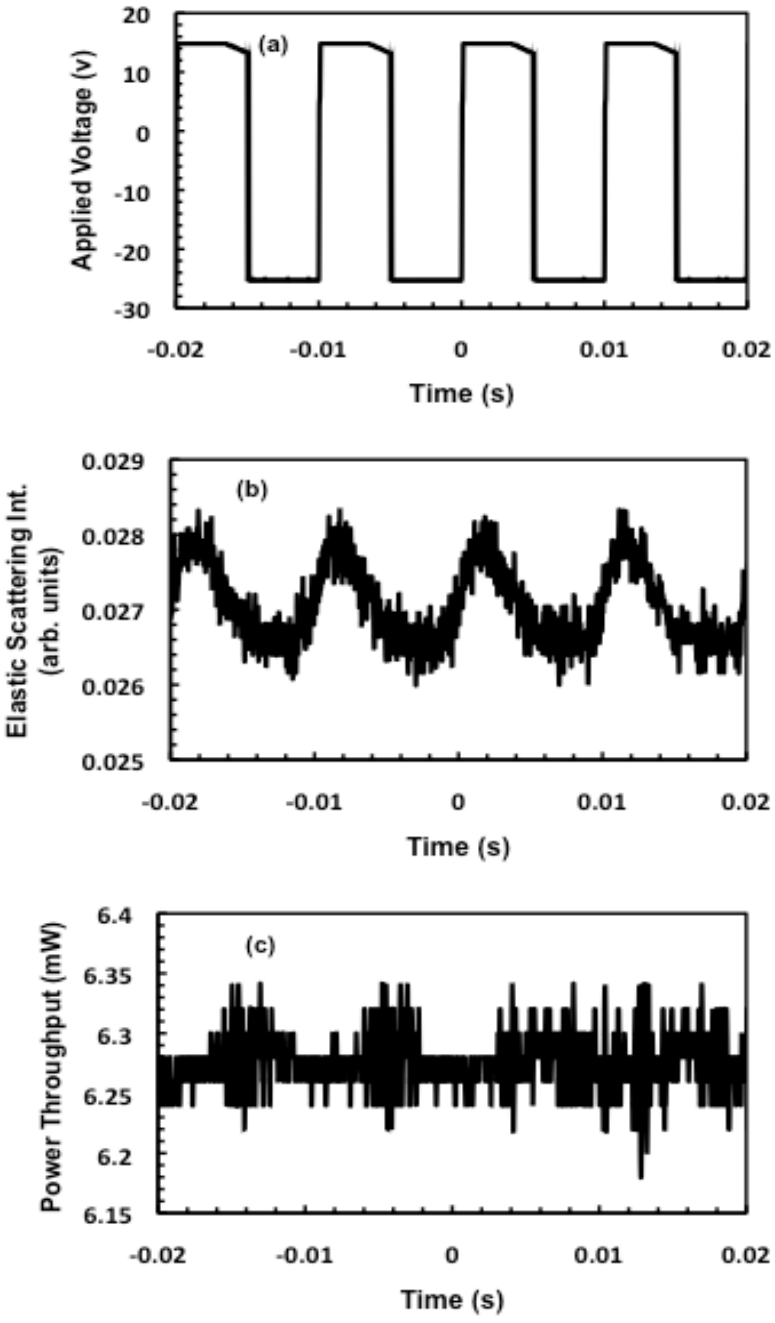

Figure 5.8 (a) Applied voltage (b) the TE polarized elastic scattering (c) transmitted signal.

As can be observed from Fig. 5.8 (b) and (c) the transmitted and scattered signal from the silicon microsphere is modulated with the applied signal. Since the modulated power throughput was hard to observe, the setup has been modified. The DFB diode laser is replaced with a high power semiconductor laser. The new semiconductor diode laser is operated at a current of 235.5 mA provided 40mW output power. The wavelength of the diode laser has been adjusted to 1545.6 nm by setting the diode laser temperature to 25.53 ^{o}C. The InGaAs PWH is replaced with a InGaAs PD, which is fed into the lock-in amplifier to clear the noise from the real signal. As shown in Fig. 5.9, an optical fiber polarization controller (PC) is placed in line with the diode laser to control the polarization of the light in the optical fiber. Furthermore, the amplifier is removed from the setup. The transmitted signal from the lock-in amplifier, the elastic scattering signal from the PD, and the input signal were all fed to a digital storage oscilloscope for signal monitoring and data acquisition. The modified setup is shown in Fig. 5.9.

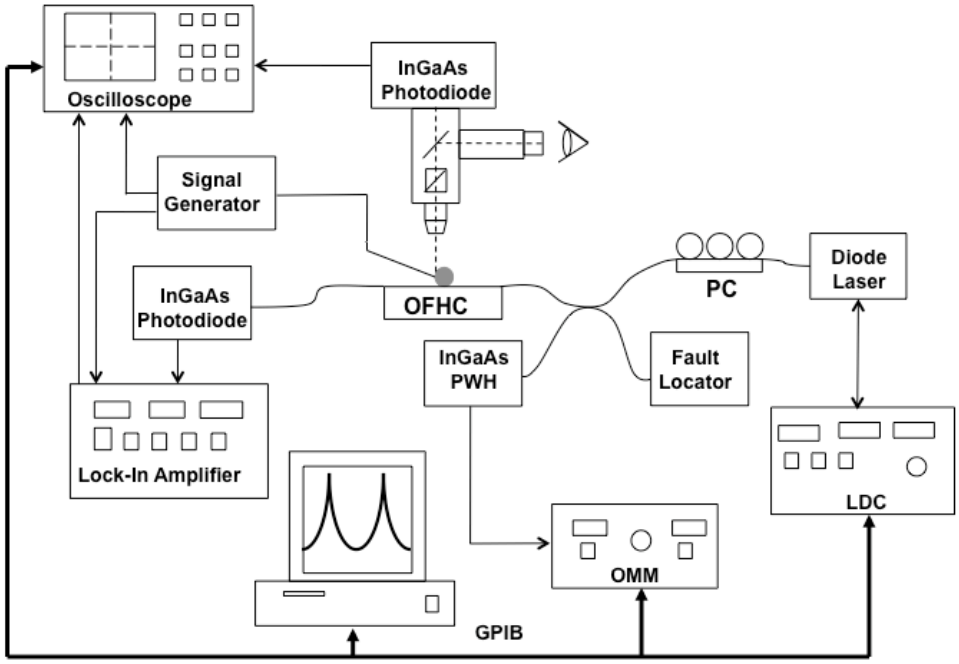

Figure 5.9 The schematic of the experimental setup.

An electrical input signal oscillating at 10 Hz between V_{min} = 5V and V_{max} = 10V is applied to the silicon microsphere, as shown in Fig. 5.10 (a) and 5.11 (a). This operating point, with a voltage modulation depth of 33% has been chosen from the IV response, shown with an arrow in Fig. 4.8. At that point the silicon microsphere conducts only when the signal is above $V_{average}$ = 7.5V. The maximum modulation frequency is on the order of 100 Hz, which is limited by the thermal response of the silicon microsphere.

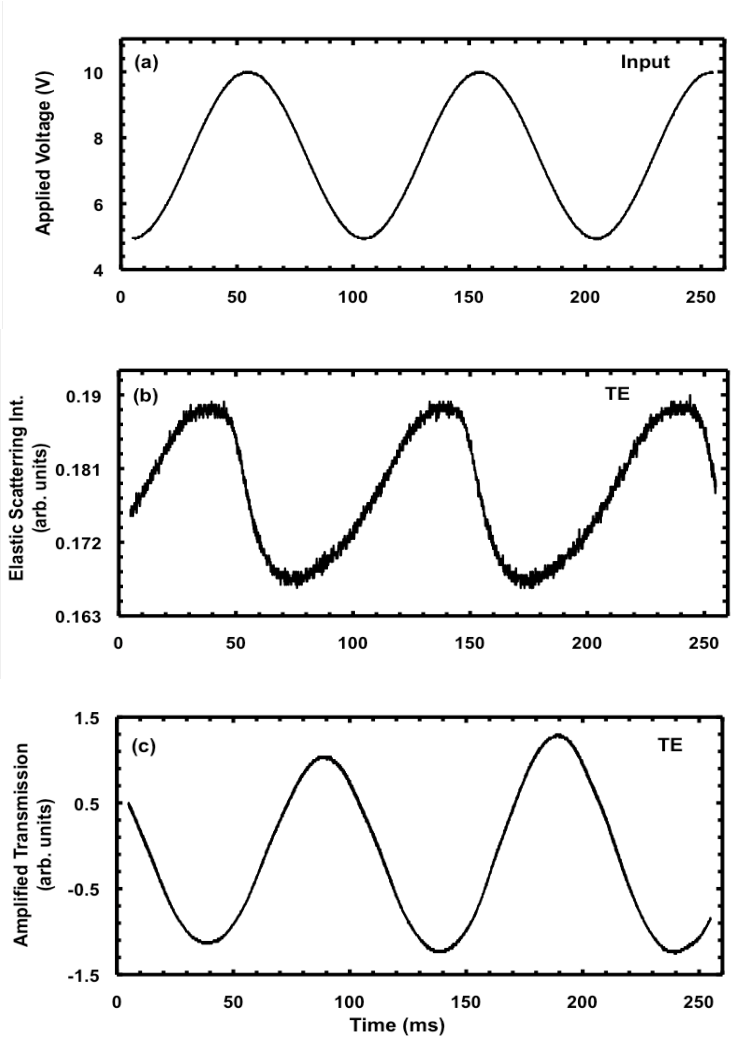

Figure 5.10 (a) Applied input signal, (b) TE polarized 90^{o} elastic scattering signal, and (c) the transmission signal from the silicon microsphere.

Fig. 5.10 (b) shows the TE polarized 90^{o} elastically scattered light from the silicon microsphere with a modulation depth of 7%, which is comparable with the modulation depth of the applied electrical signal. The transmitted optical signal from the lock-in amplifier is also shown in Fig. 5.10 (c). Both the transmitted and 90^{o} elastically scattered TE polarized light intensities are modulated at the same input frequency as the applied electrical input signal.

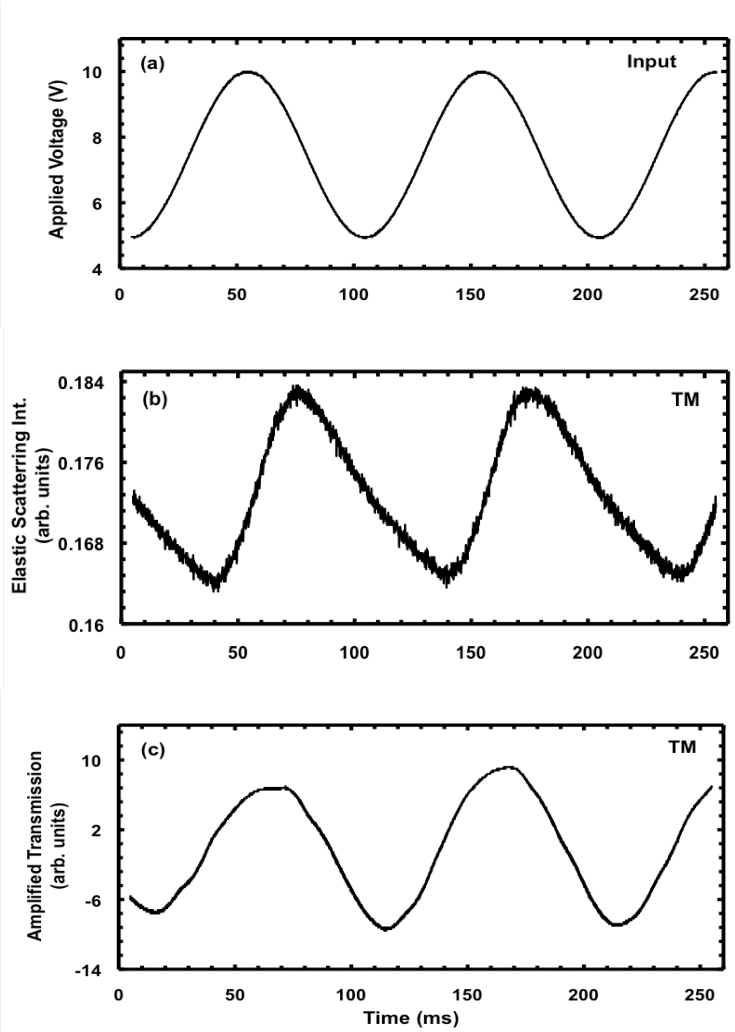

Figure 5.11 (a) Applied input signal, (b) TM polarized 90^{o} elastic scattering signal, and (c) the transmission signal from the silicon microsphere.

The same experimental procedure has been repeated for the TM polarized light. Fig. 5.11 (b) shows the TM polarized 90^o elastically scattered light from the silicon microsphere, with a modulation depth of 12%, which is at the same order of magnitude with the modulation depth of the applied electrical signal. The transmitted optical signal from the lock-in amplifier is shown in Fig. 5.11 (c).

The TE elastic scattering signal is decreasing as the current is applied to the silicon microsphere, which indicates that we are operating on the red shoulder of the TE MDR. The TM elastic scattering signal is increasing as the current is applied to the silicon microsphere, which indicates that we are operating on the blue shoulder of the TM MDR.

5.3.3 Spectroscopy with a Silicon Microsphere

Using the setup shown in Fig. 5.9 we applied square waves, with V_{min} = 0V and V_{max} = 10V at different duty cycles, to the silicon microsphere. The Glan polarizer and the PC is adjusted to select the TM polarization.

In Fig. 5.12(a) a square wave with a 3% duty cycle applied to the silicon microsphere. Later the duty cycle is increased to 6% as shown in Fig. 5.12(b). It can be observed that the TM polarized 90^o elastic scattering intensity is decreasing in Fig. 5.13(a) and (b) during the applied electrical pulse. Then the duty cycle is increased to 24%. In Fig. 5.13(c) the optical signal intensity is increasing upon the applied electrical pulse. The blue dashed lines on the Fig. 5.13 and 5.15 are representing the beginning and the end of the electrical pulse applied to the silicon microsphere. The duty cycle has been increased to 33% in Fig. 5.12(d). In Fig. 5.13(d) we observed that the TM polarized 90^o elastic scattering intensity is increasing and then decreasing during the applied electrical pulse.

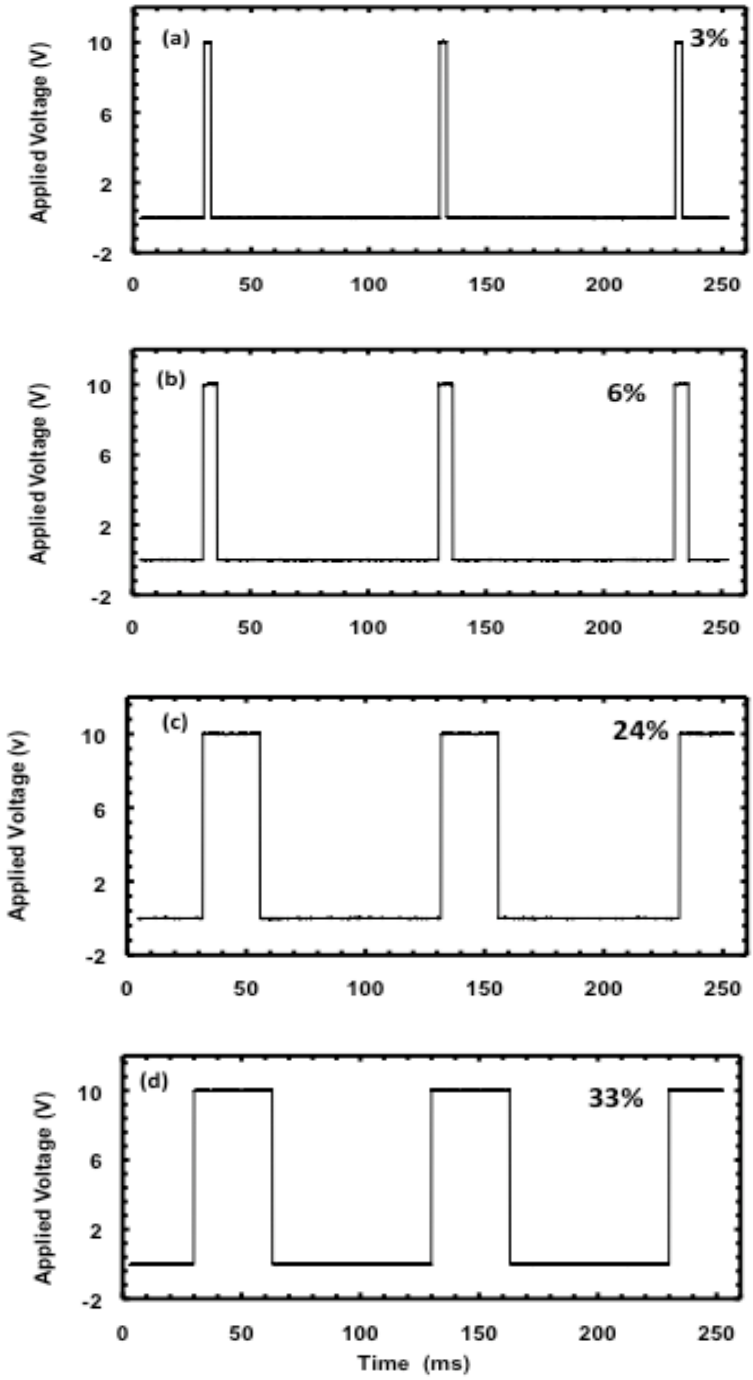

Figure 5.12. Applied voltage at (a) 3%, (b) 6%, (c) 24%, (d) 33% duty cycle.

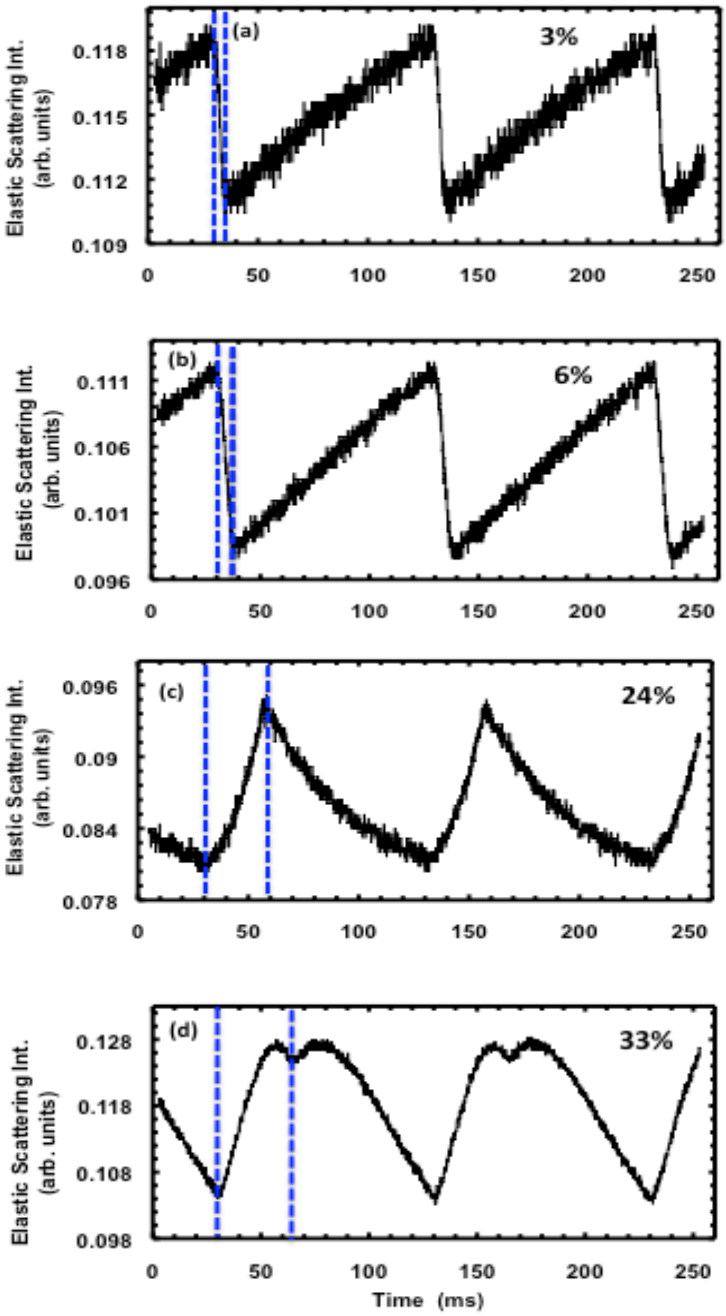

Figure 5.13 TM polarized elastic scattering light at (a) 3%, (b) 6%, (c) 24%, (d) 33% duty cycle.

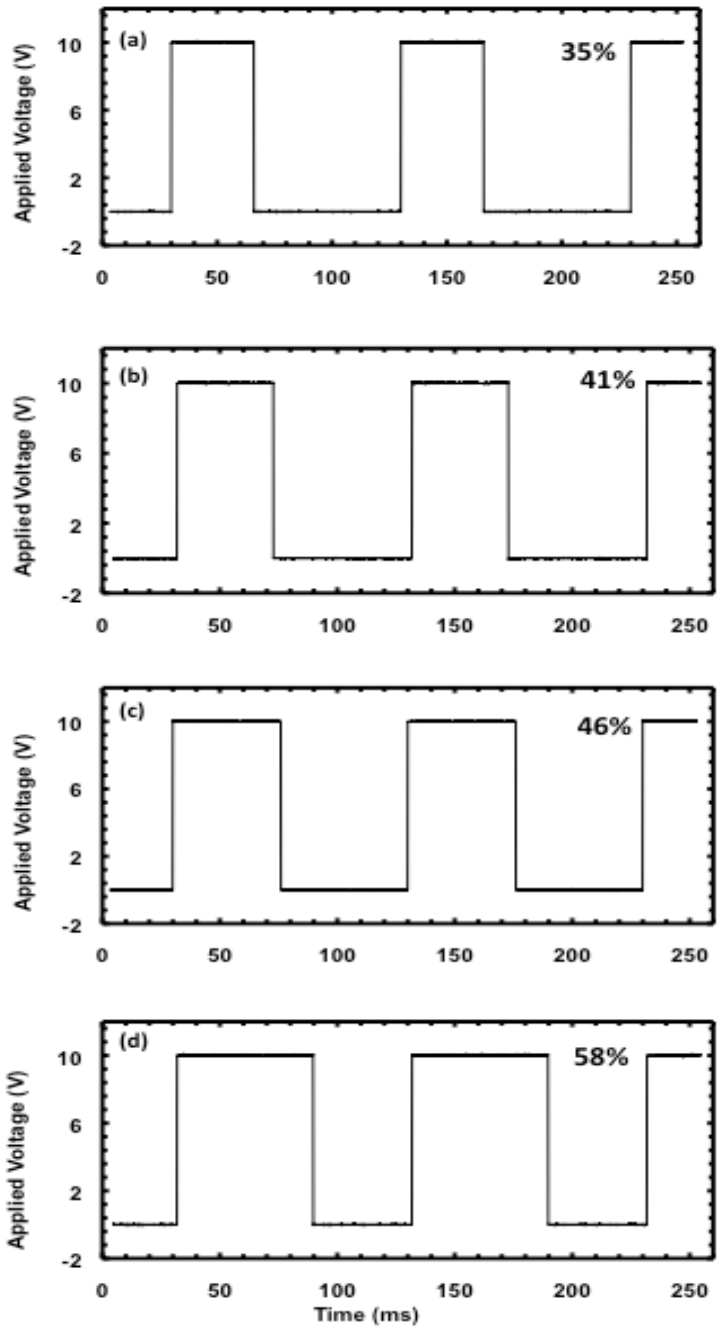

Figure 5.14 Applied voltage at (a) 35%, (b) 41%, (c) 46%, (d) 58% duty cycle.

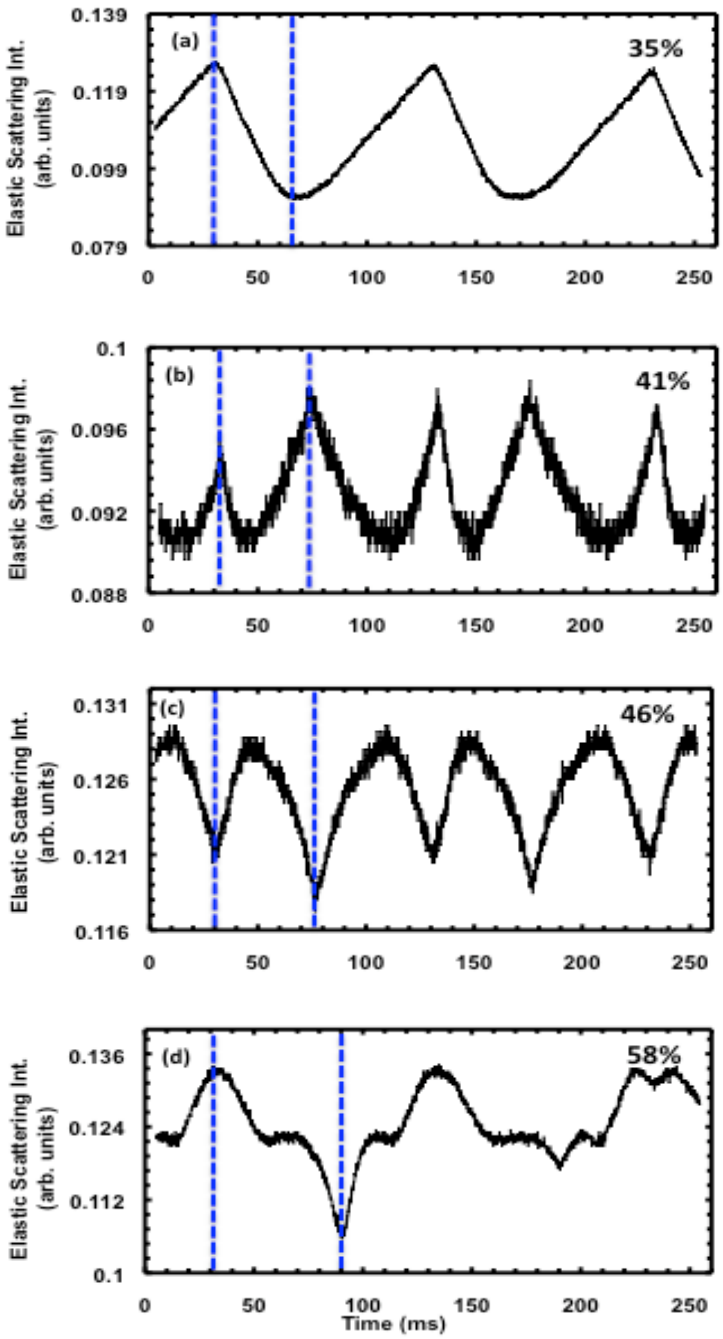

Figure 5.15 TM polarized elastic scattering light at (a) 35%, (b) 41%, (c) 46%, (d) 58% duty cycle.

In Fig. 5.14(a) the electrical signal with a 35% duty cycle applied to the silicon microsphere. Later the duty cycle is increased to 41% as shown in Fig. 5.14(b). It can be observed that the TM polarized 90^o elastic scattering intensity is decreasing in Fig. 5.15(a) during the electrical pulse. Then a voltage with a duty cycle of 46% is applied to the sphere as shown in Fig. 5.14(c). In Fig. 5.15(b) the optical signal is on its local minimum whereas in Fig. 5.15(c) the optical signal is on its local maximum, when the pulse is applied to the silicon microsphere. The duty cycle is increased to 58% in Fig. 5.14(d). The TM polarized 90^o elastic scattering signal at 58% duty cycle is shown in Fig. 15(d).

In table 5.1 the modulation depths of the elastic scattering intensities, the time of the applied voltage duration, and the shift in the MDR's are given at different duty cycles.

Table 5.1 Modulation depth, time duration and shift in MDR's at different duty cycles.

Parameter	**Units**	**Values**							
Duty Cycle	**(%)**	3	6	24	33	35	41	46	58
Modulation Depth	**(%)**	7	10	16	19	31	8.5	9.7	20
Time Duration	**(ms)**	3	6	24	33	35	41	46	58
Shift	**(nm)**	0.0012	0.0024	0.0096	0.013	0.014	0.016	0.018	0.023

5.4 Discussions

In Figs. 5.13 and 5.15, the TM polarized 90^o elastic scattering intensity is exhibiting various shapes, which mirrors itself in on and off times of the applied square wave. This behavior is due to the change in the refractive index of the silicon microsphere. The

refractive index changes during the on-time, and recovers to its initial value during the off-time. It can be observed that the scattered signal is increasing or decreasing during the applied voltage. This phenomenon is illustrated in Fig. 5.16. When current is injected, MDR's shifts in wavelength. At a constant laser wavelength, we move from the dashed curve to the solid curve. As a result the elastic scattering intensity is increasing. As the duty cycle increases, the shapes get more complicated and last longer as the microsphere scans different parts of a MDR spectrum.

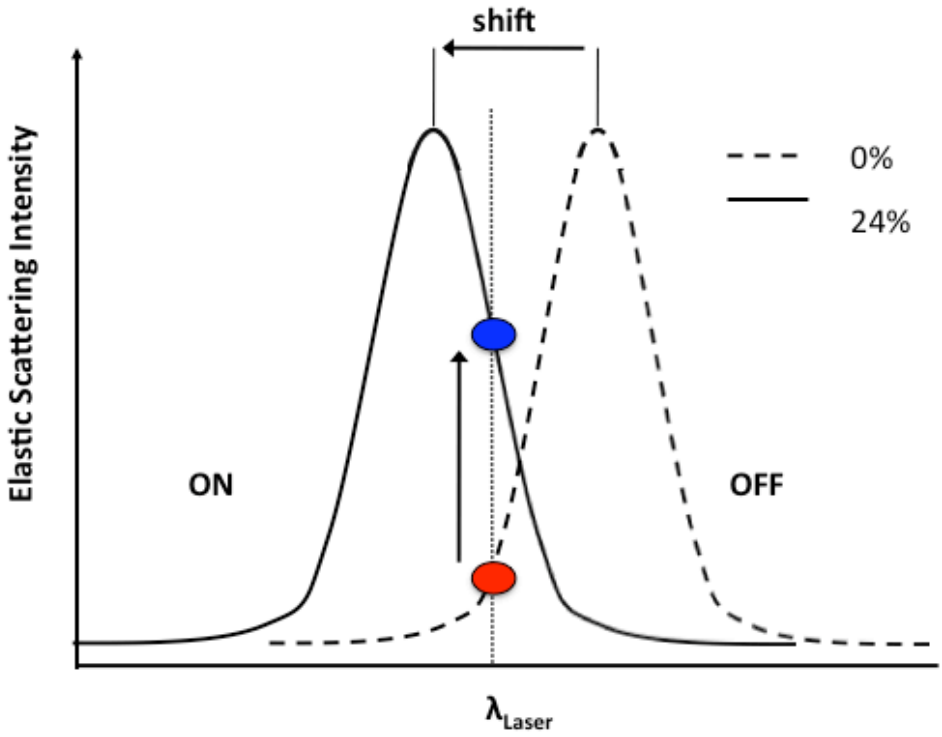

Figure 5.16 The shift of MDR's as a result of current injection.

In Fig. 5.17, we combined the elastic scattering intensities in between the dashed lines of Fig. 5.14 and 5.15 in order to form a mosaic spectrum.

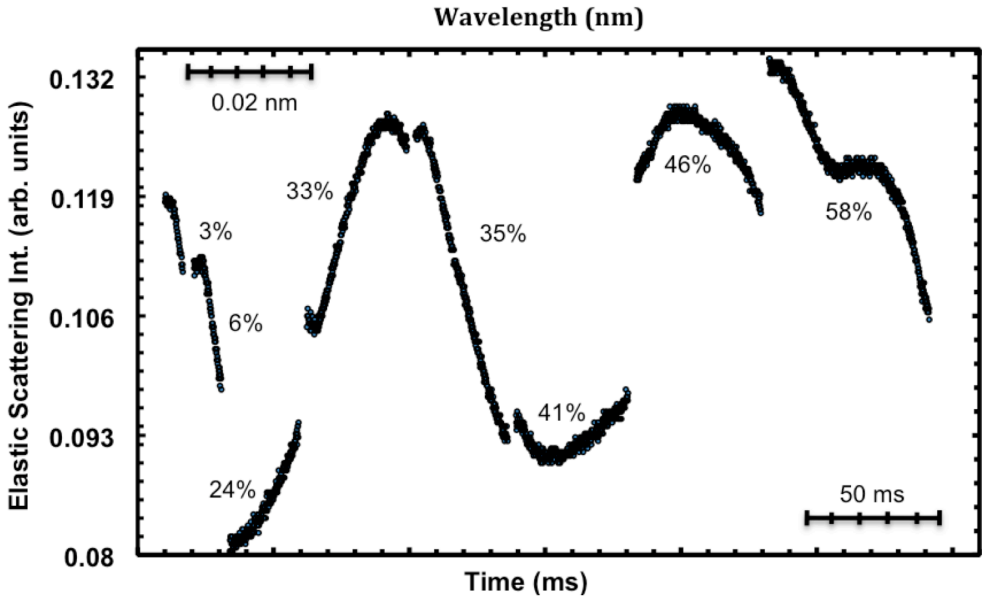

Figure 5.17 The combined elastic scattering spectra at increasing duty cycles.

Lastly, we applied a square wave at slower rates and at 30% duty cycle, shown in Fig. 5.18 (a), in order to observe the MDR spectrum completely. At slower rates we were able to observe the change the in the refractive index of the silicon microsphere. The elastic scattering from the silicon microsphere is shown in Fig. 5.18 (b). In Fig. 5.18 (c), the refractive index change and in Fig. 5.18 (d) the recovery of the refractive index change is shown. As a result, optical spectroscopy can be performed by current tuning the silicon microsphere, as shown in Fig. 5.18.

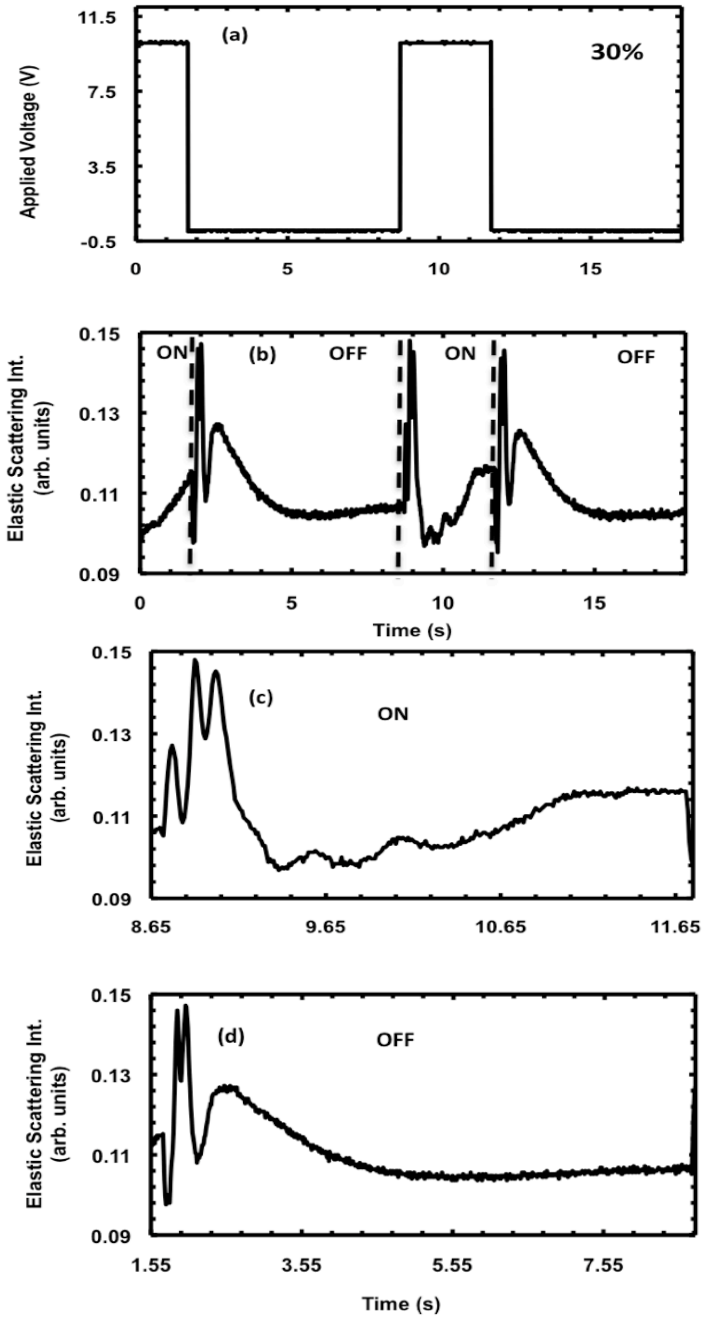

Figure 5.18 (a) Applied voltage (b) elastic scattering intensity at 30% duty cycle, while the source is on (c) and off (d).

5.4.1 Electro-optical Analysis

In Fig. 5.17, the elapsed time $\delta t = 50$ ms is matched to a wavelength shift of $\delta\lambda = 0.02$ nm using the following procedure. The wavelength shift $\delta\lambda$ can be estimated using the proportionality between relative wavelength shift $\delta\lambda$ and the relative refractive index shift δm given by

$$\frac{\delta\lambda}{\lambda} = \frac{\delta m}{m} \tag{5.1}.$$

The refractive index of the silicon microsphere changes according to [39]

$$\delta m = -\frac{e^2\lambda_0^2}{8\pi^2 c^2 \varepsilon_0 m}\left(\frac{\delta N_e}{m_{ce}^*} + \frac{\delta Nh}{m_{ch}^*}\right) \tag{5.2},$$

where $m = 3.5$ is the refractive index, e the elementary charge, $\lambda = 1.55$ μm the vacuum wavelength, c the speed of the light in vacuum, ε is the permittivity of the vacuum, δN_e the change in the number of the electrons, δN_h the change in number of holes, m_{ce}^* the conductivity effective mass of electrons, and m_{ch}^* the conductivity effective mass of holes. The conductivity effective mass $m_{ce}^* = 0.26\ m_0$ and $m_{ch}^* = 0.39\ m_o$, where m_o is the electron mass [40].

Therefore, substituting the constants in Eq.5.2 for the electrons gives the relation between refractive index change and the concentration of free electrons.

$$\delta m = -8.8\times10^{-22}\delta N_e \tag{5.3}.$$

The relation between refractive index change and the concentration of free holes is

$$\delta m = -8.5\times10^{-18}(\delta N_h)^{0.8} \tag{5.4}$$

Moreover, the current is given by

$$I = \frac{\delta Q}{\delta t} = eV\frac{\delta N}{\delta t} \quad (5.5),$$

where Q is the total charge, δt the on-time, V the volume of the spherical shell for the current flow, and δN is the number of free carriers. As a result δN is given by

$$\delta N = \frac{I\delta t}{eV} \quad (5.6).$$

The relation between the relative wavelengths shift in time can be find using Eq. 5.3 and Eq. 5.5 in Eq. 5.1, for electrons.

$$\delta\lambda = -\frac{\lambda}{m}8.8\times10^{-22}\frac{I}{e4\pi a^2 d}\delta t \quad (5.7),$$

The same procedure can be followed for holes.

$$\delta\lambda = -\frac{\lambda}{m}8.5\times10^{-18}\left(\frac{I}{e4\pi a^2 d}\delta t\right)^{0.8} \quad (5.8)$$

where d is the penetration depth of the free carriers and a the radius of the microsphere. The δm calculated using Eq. 5.6 matches the on-time δm shown in Fig. 5.17. Fig. 5.19 shows the flow of free carriers.

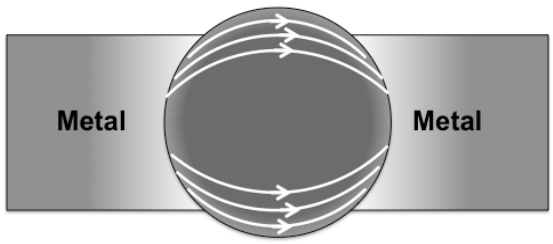

Figure 5.19 Proposed model of the current flow in the silicon microsphere.

5.4.2 Thermo-optic Analysis

In order to find the relation between the wavelength shift and temperature change, Eq. 5.1 is rearranged and multiplied by 1/δt,

$$\frac{1}{\delta t}\delta\lambda = \frac{1}{\delta t}\delta m\frac{\lambda}{m} \tag{5.9},$$

where t is the total operation time. Then the right side of Eq. 5.9 is multiplied by δT/δT

$$\frac{\delta\lambda}{\delta t} = \frac{\delta m}{\delta t}\frac{\lambda}{m}\frac{\delta T}{\delta T} = \frac{\lambda}{m}\frac{\delta m}{\delta T}\frac{\delta T}{\delta t} \tag{5.10}$$

where T is the temperature. Moreover, according to heat conduction model, the thermal power is given by

$$P = \frac{\Delta TA}{L/k_{si}} \tag{5.11},$$

where A is the area, L the length and k_{si} = 1.56W/cm/K the thermal conductivity of silicon.

The duty cycle can be related to the change in the temperature by Eq. 5.12.

$$Duty\ Cycle = \frac{\delta t}{t} = \frac{\delta T}{\Delta T} \Rightarrow \frac{\Delta T}{t} = \frac{\delta T}{\delta t} \tag{5.12}.$$

Rearranging Eq. 5.11 and dividing by t, we can get Eq. 5.13.

$$\frac{\delta T}{\delta t} = \frac{PL}{Ak_{si}t} \tag{5.13}$$

Lastly, inserting Eq. 5.13 into Eq. 5.10 will result into

$$\frac{\delta\lambda}{\delta t} = \frac{\lambda}{m}\frac{\delta m}{\delta T}\frac{PL}{Ak_{si}t} \tag{5.14}.$$

Inserting the constants, and Eq. 3.7 into Eq. 5.14 will give us the relation between time and wavelength, for thermal effects.

$$\delta\lambda = 8.3\times10^{-4}\,\delta t \tag{5.15}.$$

For δt = 50ms gives as δλ = 0.04 pm, which is smaller than the observed shifts, which seem to result from a combination of thermal and electrical effects.

Chapter 6

CONCLUSIONS AND FUTURE WORK

In this work, after a revision of Fabry-Perot resonators, microsphere resonators are discussed by using Lorenz-Mie theory. Later, the mode spacing of MDR's and *Q-factor* are discussed. Optical modulation mechanisms in silicon are explained. Later, the electrical characterization of the silicon microsphere is discussed by giving the theory and experimental results. The maximum current on the sphere at 10V is found to be 5μA and the maximum power dissipated on the silicon microsphere is found to be 250μW.

Moreover, the MDR's of a silicon microsphere placed on an OFHC have been excited by a temperature tunable DFB semiconductor diode laser. MDR peaks and corresponding dips have been observed in the elastic scattering spectra and the transmission spectra, respectively. In this work, we have obtained a mode spacing value of $\Delta\lambda = 0.32$ nm and a mode linewidth of $\delta\lambda = 0.18$ nm leading to a quality factor of 10^4. Furthermore, we have demonstrated an optical modulator using a silicon microsphere evanescently coupled to an optical fiber half coupler. As a result of applied electrical signal, the elastically scattered and the transmitted optical signals are modulated at 10Hz for both the TE and the TM polarization geometries.

Finally, we have demonstrated optical spectroscopy using a silicon microsphere in an modulator configuration. The silicon microsphere is evanescently coupled to an optical fiber half coupler. As a result of applied electrical signal, the TM polarized elastically scattered and the transmitted optical signals are modified. The MDR peaks in the TM polarized elastic scattering spectra can be observed by current tuning the silicon microsphere. The tuning of the silicon microsphere resulted in a shift of MDR's around 0.023 nm at 58% duty cycle.

As a future work, a p-n type silicon microsphere could increase the carrier injection level, which will result in bigger shifts of the MDR's.

APPENDIX A

A.1 Virtual Instruments

In this section the virtual instruments (VI's) are developed using LabView® is explained. Before using the VI's make sure that the latest driver library is installed on the computer. The driver libraries (VISA) suitable with the LabView® can be downloaded from the national instruments web site. Moreover, USB to serial port convertors are used to control the power supplies via serial port. The driver of the convertors also has to be installed beforehand.

A.1.1 Current - Voltage Measurement VI

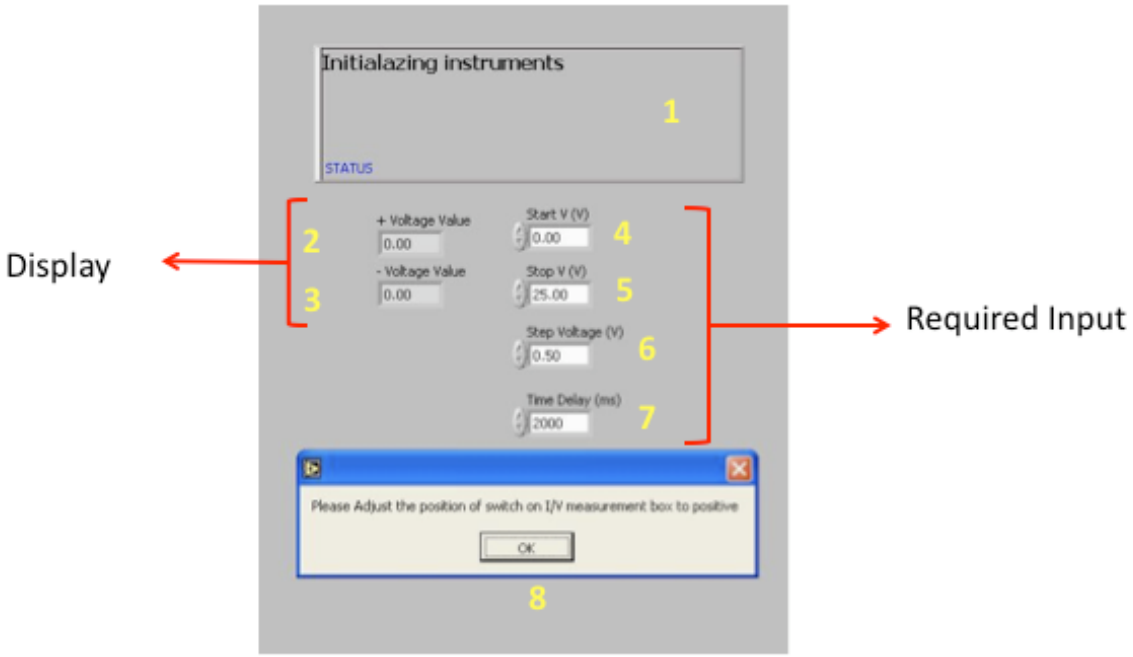

Figure A.1.1.1 I-V Measurement VI front panel.

This VI is developed in order to carry out the I-V measurements. Before clicking the run button the required fields have to be filled. All the data output is saved under Shared/Measurement folder with the date and time as the file name. The list of the boxes in the Fig. A.1.1.1 is given below.

1: Status; will tell you the current progress and also will give you instructions when the user input is needed.

2: + Voltage Value; will display the voltage on the sample when positive voltage is applied.

3: - Voltage Value; will display the voltage on the sample when negative voltage is applied.

4: Start Voltage; is the voltage value that you want to start in.

5: Stop Voltage; is the voltage value that you want to stop in.

6: Step Voltage; is the step voltage value that is going to be used to reach stop voltage value.

7: Time Delay; is the delay that you want to wait at each step in ms.

8: Dialog window; appears when the user input is needed. In this VI it will appear at first to notify you to switch the polarity to positive on the I-V measurement box. In the middle of the program it will appear again to tell the user to switch the polarity on the I-V box to negative.

A.1.2 MDR Spectrum VI

This VI is developed in order to carry out MDR spectra. Before clicking the run button the required fields have to be filled. This VI has a different logic than the other ones used previously. The previous VI's developed used to scan the temperature of the laser by controlling the temperature directly. Whereas this VI is developed to control the temperature by tuning the peltier cooler current which provides better temperature control.

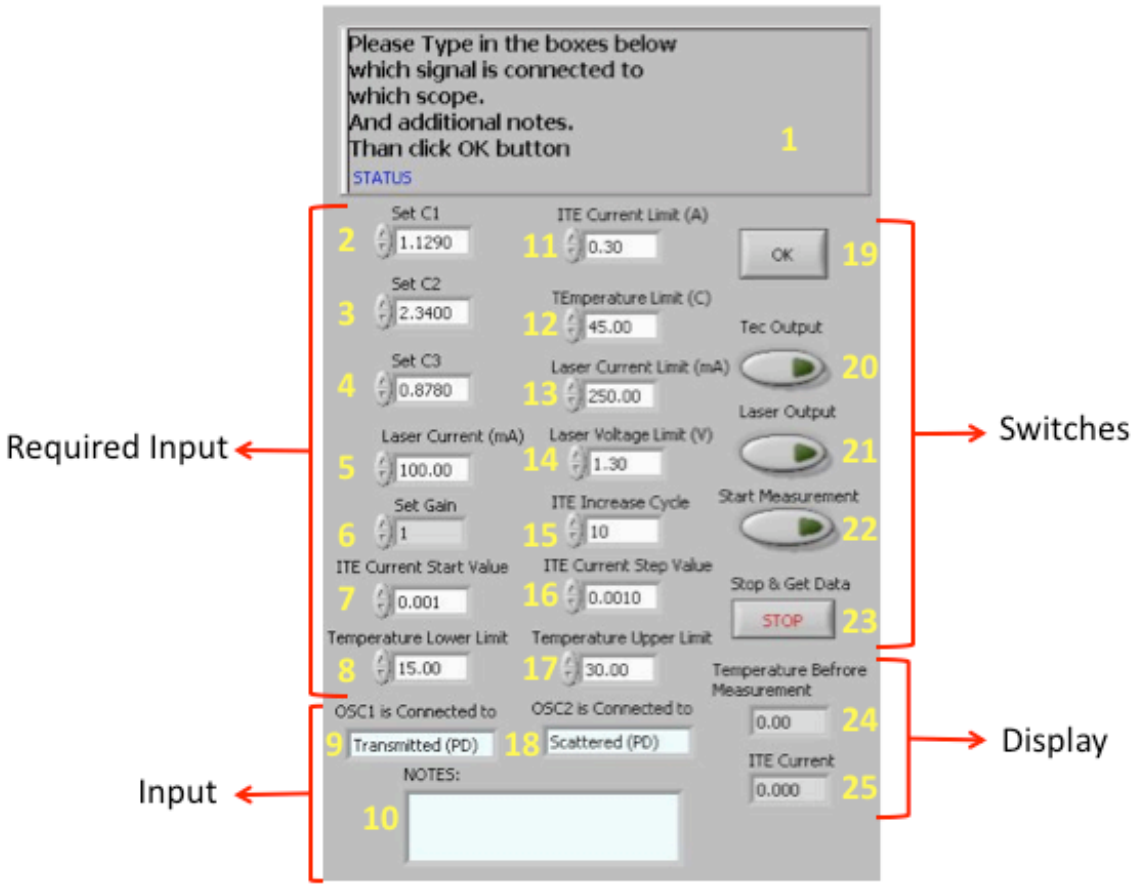

Figure A.1.2.1 The front panel of MDR spectrum VI.

All the data output is saved under Shared/Measurement folder with the date and time as the file name. The list of the boxes in the Fig. A.1.2.1 will give you the detailed information about each box.

1: Status; will tell you the current progress and also will give you instructions when the user input is needed.

2: Set C1; write the C1 value for the thermocouple of the laser holder.

3: Set C2; write the C2 value for the thermocouple of the laser holder.

4: Set C3; write the C3 value for the thermocouple of the laser holder.

5: Laser Current; write current value that you want to operate the laser in mA. Refer to the manual of the laser for upper limit.

6: Set Gain; is the gain of the temperature controller. This value determines how fast the temperature is set to target temperature value.

7: ITE Current Start Value; is the start current value of the TEC controller. This value should be kept small. Since smaller current is desired for smaller temperature change. However, if the measurement starts from a temperature different than the start temperature, this value should be increased. Since the driving current of TEC is not enough to keep the temperature at the start temperature, this value can be increased if desired. Refer to the laser holder manual for the upper limit.

8: Temperature lower limit; is the temperature that the scan is going to stop.

9: OSC 1 is connected to; whatever you type here will be written on top of the data file for the relevant column. That is, if the channel 1 one of the oscilloscope 1 is connected to the PD at the scattered signal, write here scattered. This string is going to be written in the output file at the top of the scattered signal data. This field is not required. However, if you want it to ne added at the output file it has to be filled before you click OK button.

10: Notes; you can write any note here that is going to added at the end of the parameter file. For instance, it can be the temperature of the environment or the polarization of the light. This field is not required. However, if you want it to ne added at the output file it has to be filled before you click OK button.

11: ITE Current Limit; the upper current limit of the TEC controller. Refer to the laser holder manual.

12: Temperature Limit; the upper temperature limit of the laser. Refer to the laser manual.

13: Laser Current Limit; the upper current limit of the laser. Refer to the laser manual.

14: Laser Voltage Limit; the upper voltage limit of the laser. Refer to the laser manual.

15: ITE increase cycle: can be used to obtain more data. If you type 4 here, the program will tale 4 data points and then will increase the ITE current. At each step it will take 4 data points, instead of 1.

16: ITE current step value; is the step current value that is going to be used to reach stop temperature.

17: Temperature upper limit; is the upper temperature limit for the laser. Refer to laser manual.

18: OSC 2 is connected to; whatever you type here will be written on top of the data file for the relevant column. That is, if the channel 1 one of the oscilloscope 2 is connected to the PD at the transmitted signal, write here transmitted. This string is going to be written in the output file at the top of the scattered signal data. This field is not required. However, if you want it to ne added at the output file it has to be filled before you click OK button.

19: OK; the program won't proceed until you click to this button. Make sure you click it when every parameter is correctly typed.

20: TEC output; will turn on the temperature controller output at the LDC.

21: Laser output; will turn on the laser output at the LDC.

22: Start Measurement; will start the measurement.

23: Stop & get data; enables to get the data collected till you click. Different from the stop button in LabView® menu, this can give you the data output. If you click on stop button in LabView® menu you won't be able to get data output file.

24: Temperature before measurement; displays the temperature of the laser before you click on start button. Later the temperature is displayed on the waveform chart.

25: ITE current; displays the current ITE current value.

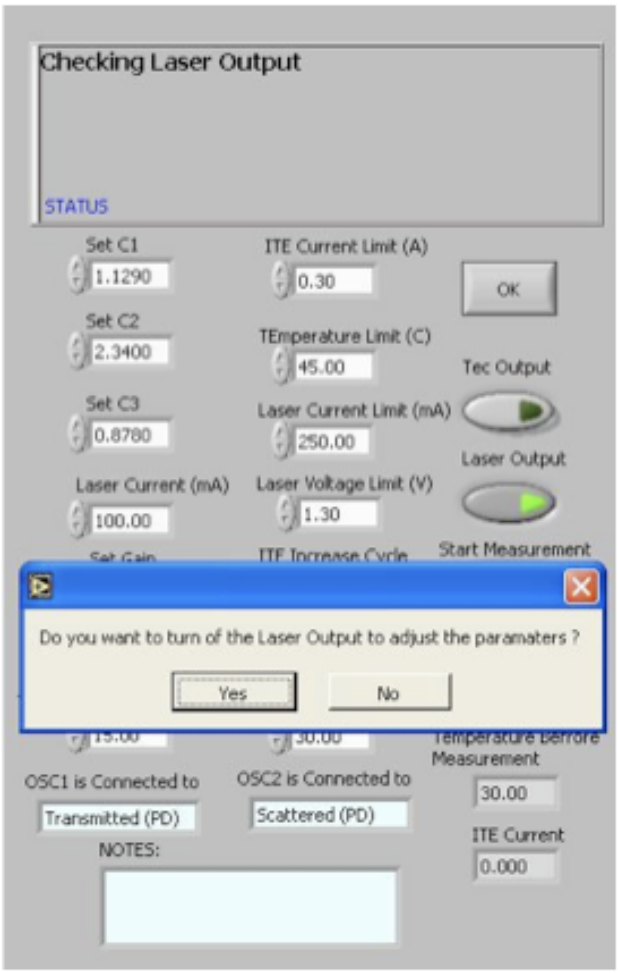

Figure A.1.2.2 The front panel of MDR spectrum VI during measurement.

MDR spectrum VI is designed not to turn off the laser at each measurement. As a result, the lifetime of the laser can be increased. Moreover, the laser will be more stable. After your first measurement a dialog box will appear. It will ask you ‘’Do you want to turn of the laser output to adjust the parameters?’’. Click no if you did not make any changes in laser parameters. However, if you made changes any parameter in box 5, 13, 14, say yes to the dialog box.

A.1.3 Oscilloscope Screen Capture VI

This VI is developed in order to capture the waveform displayed on the screen of two oscilloscopes. Unlike the other VI's this VI does not control the devices. It only acquires the waveform from the oscilloscopes. Other than the modulation experiment this VI can be used to capture any waveform on the scope. All the data output is saved under Shared/Measurement folder with the date and time as the file name.

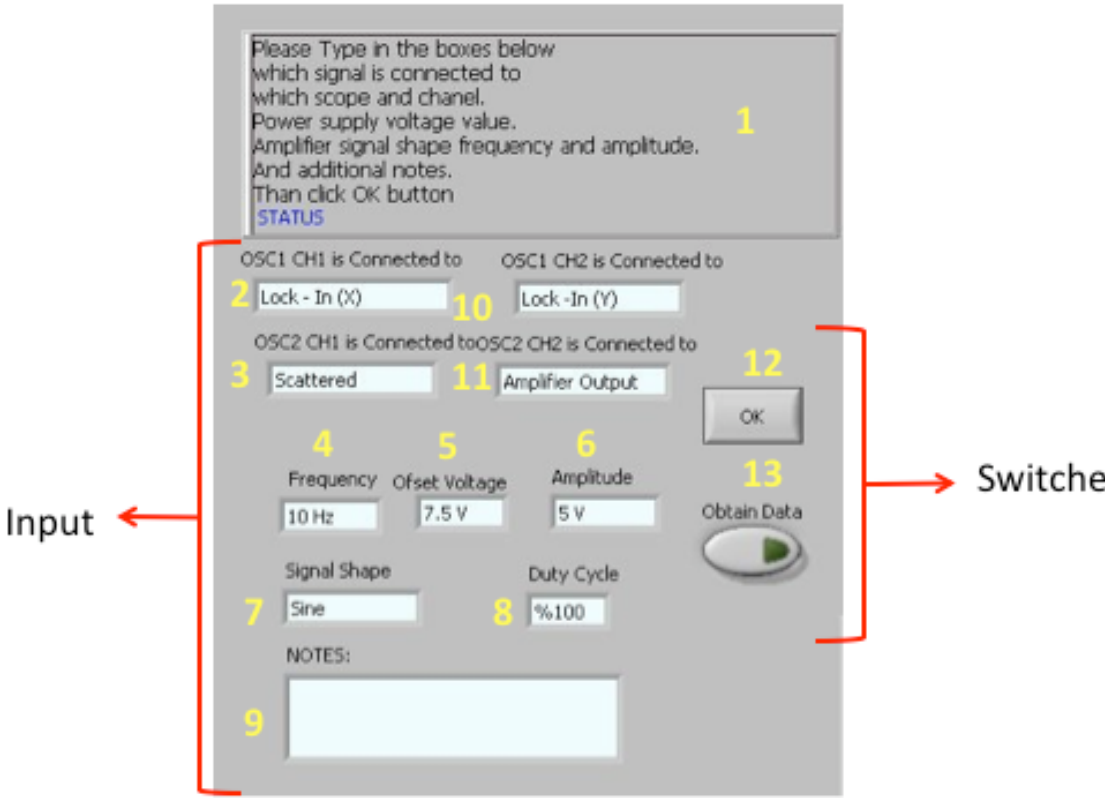

Figure A.1.3.1 The front panel of the OSC capture VI.

The list of the boxes shown in Fig. 4.1.3.1 is given below in order to give detailed information about the operation of the program.

1: Status; will tell you the current progress and also will give you instructions when the user input is needed.

2: OSC1 CH1 is connected to; whatever you type here will be written on top of the data file for the relevant column obtained from channel 1 of oscilloscope 1 . This field is not required. However, if you want it to ne added at the output file it has to be filled before you click OK button.

3: OSC2 CH1 is connected to; whatever you type here will be written on top of the data file for the relevant column obtained from channel 1 of oscilloscope 2 . This field is not required. However, if you want it to ne added at the output file it has to be filled before you click OK button.

4: Frequency; can be filled if you want the frequency information to be added to the parameter file.

5: Offset Voltage; can be filled if you want the offset voltage information to be added to the parameter file.

6: Amplitude; can be filled if you want the amplitude information to be added to the parameter file.

7: Signal Shape; can be filled if you want the signal shape information to be added to the parameter file.

8: Duty Cycle; can be filled if you want the duty cycle information to be added to the parameter file.

9: Notes; you can write any note here that is going to be added at the end of the parameter file. For instance, it can be the polarization of the light. This field is not required. However, if you want it to ne added at the output file it has to be filled before you click OK button.

10: OSC1 CH2 is connected to; whatever you type here will be written on top of the data file for the relevant column obtained from channel 2 of oscilloscope 1. This field is

not required. However, if you want it to ne added at the output file it has to be filled before you click OK button.

11: OSC2 CH2 is connected to; whatever you type here will be written on top of the data file for the relevant column obtained from channel 2 of oscilloscope 2. This field is not required. However, if you want it to ne added at the output file it has to be filled before you click OK button.

12: OK; click this button after you finish typing the input fields.

13: Obtain Data; starts the data acquisition. You will be notified, when it finishes.

VITA

Emre Yüce was born in Erzurum, Turkey in 1983. He completed the high school in İbrahim Hakkı Fen Lisesi, Erzurum, in 2001. He received his B. Sc. degree in Physics from Middle East Technical University (METU), Ankara, Turkey, in 2007. He worked on ‘’Crystal growth by Bridgman Stockbarger Technique’’ at METU as his undergraduate thesis with Prof. Bülent Akınoğlu. He joined the M.Sc. program in Physics at Koç University in Istanbul, Turkey in 2007, as a teaching/research assistant during which, he worked on “Optical Modulation and Spectroscopy with Silicon Microspheres” with Prof. Ali Serpengüzel. As of fall 2009, he will continue his Ph.D. work at Atomic and Molecular Physics Institute (AMOLF), Amsterdam, The Netherlands. He is expected to work with Prof. Willem L. Vos on ‘’Advanced quantum optical measurements of the transport and emission of light in nanostructures for ultrafast modulation and switching’’.

BIBLIOGRAPHY

[1] L. Pavesi, “Will silicon be the photonic material of the next millennium?,” J. Phys., Condensed Matter, 15, 1169 (2003).

[2] C.A. Barrios and M. Lipson, “Silicon Photonic Read Only Memory,” J. Lightwave Technol., 24, 7 (2006).

[3] R. Jones, H. Rong, A. Liu, A. Fang, and M. J. Paniccia, "Net Continuous Wave Optical Gain in a Low Loss Silicon-on-Insulator Waveguide by Stimulated Raman Scattering," Opt. Express 13, 519 (2005).

[4] P.W. Barber and R.K. Chang, Optical Effects Associated with Small Particles, World Scientific, Singapore, pp. 3-61 (1988).

[5] K. Totsuka and M. Tomita, “Dynamics of fast and slow pulse propagation through a microsphere–optical-fiber system,” Phys. Rev. A 75, 016610 (2007).

[6] Y.O. Yılmaz, A. Demir, A. Kurt and A. Serpengüzel, “Optical Channel Dropping with a Silicon Microsphere,” IEEE Photon. Technol. Lett. 17, 1662 (2005).

[7] H. C. Tapalian, J. -P. Laine, and P.A. Lane, ‘’Thermooptical switches using coated microsphere resonators,’’ IEEE Photon. Technol. Lett., 14, 1118 (2002).

[8] A. Tewary, M.J.F. Digonne, J.Y. Sung, J.H. Shin and M.L. Brongersma, ‘’Silicon-nanocrystal-coated silica microsphere thermooptical switch,’’ IEEE J. Sel. Top. Quantum Electron., 12, 1476 (2006).

[9] L. Liao, A. Liu, R. Jones, D. Rubin, D. Samara-Rubio, O. Cohen, M. Salib and M. J. Paniccia, "Phase Modulation Efficiency and Transmission Loss of Silicon Optical Phase Shifters," IEEE J. Quantum Electron. 41, 250 (2005).

[10] A. Liu, R. Jones, L. Liao, D. Samara-Rubio, D. Rubin, O. Cohen, R. Nicolaescu, M. J. Paniccia, "A High-Speed Silicon Optical Modulator based on a Metal-Oxide-Semiconductor Capacitor," Nature, 427, 615 (2004).

[11] L. Liao, D. Samara-Rubio, M. Morse, A. Liu, D. Hodge, D. Rubin, U. D. Keil, and T. Franck, "High Speed Silicon Mach-Zehnder Modulator," Opt. Express 13, 3129 (2005).

[12] R. Jones, A. Liu, H. Rong, M. J. Paniccia, O. Cohen, and D. Hak, "Lossless Optical Modulation in a Silicon Waveguide using Stimulated Raman Scattering," Opt. Express 13, 1716 (2005).

[13] Q. Xu, S. Manipatruni, B. Schmidt, J. Shakya, and M. Lipson, "12.5 Gbit/s carrier-injection-based silicon microring silicon modulators," Opt. Express 15, 431 (2007).

[14] I. Kiyat, A. Aydinli, N. Dagli, ''Low-power thermooptical tuning of soi resonator switch,'' IEEE Photon. Technol. Lett., 18, 364 (2006)

[15] L. Zhou and A. W. Poon, ''Silicon electro-optic modulators using p-i-n diodes embedded 10-micron-diameter microdisk resonators,'' Opt. Express, 14, 6851 (2006).

[16] A. Liu, L. Liao, D. Rubin, H. Nguyen, B. Ciftcioglu, Y. Chetrit, N. Izhaky and M. Paniccia, '' High-speed optical modulation based on carrier depletion in a silicon waveguide,'' Opt. Express, 15, 660 (2007).

[17] L. Gu, W. Jiang, X. Chen and R. T. Chen, ''Physical mechanism of p-i-n-diode-based photonic crystal silicon electrooptic modulators for gigahertz operation'' IEEE J. Sel. Top. Quantum Electron., 14, 1132 (2008).

[18] B.E. Little, S.T. Chu, H.A. Haus, J. Foresi, J.P. Laine, ''Microring resonator channel dropping filters,'' IEEE Lightwave Tech., 15, 998 (1997).

[19] J. Yao, D. Leuenberger, M. C. M. Lee, and M. C. Wu, ''Silicon Microtoroidal Resonators With Integrated MEMS Tunable Coupler,'' operation'' IEEE J. Sel. Top. Quantum Electron., 13, 202 (2007).

[20] K. Djordjev, S. J. Choi, P. D. Dapkus, '' High-Q vertically coupled InP microdisk resonators,'' IEEE Photon. Tech. Lett., 14, 331 (2002).

[21] M. L. Gorodetsky, A. A. Savchenkov, and V. S. Ilchenko ''Ultimate Q of optical microsphere resonators,'' 21, 453 (1996).

[22] M. Born and E. Wolf, ‘’Principles of Optics,’’ Cambridge University Press, New York, (1999).

[23] L. Rayleigh, “The problem of the whispering gallery,” Scientific Papers 5, 617 (1912).

[24] A. Serpengüzel, S. Arnold, G. Griffel, J.A. Lock, “Enhanced Coupling to Microsphere resonances with optical fibers,” J. Opt. Soc. Am., 14, 790 (1997).

[25] B.R. Johnson, “Morphology-dependent resonances of a dielectric sphere on a conducting plane,” J. Opt. Soc. Am., 11, 2055 (1994).

[26] T. Bilici, S. İşçi, A. Kurt and A. Serpengüzel, “Microsphere-Based Channel Dropping Filter with an Integrated Photodetector,” IEEE Photon. Tech. Lett. 16, 476 (2004).

[27] H.C. Hulst, van de, Light Scattering by Small Particles, Dover, New York (1981).

[28] P. Barber, and S. C. Hill, Light Scattering by Particles: Computational Methods World Scientific, Singapore (1990).

[29] B. E. Little, J. P. Laine, and H. A. Haus, “Analytic theory of coupling from tapered fibers and half-blocks into microsphere resonators.” Journal of Lightwave Technol. vol.17, 704 (1999).

[30] P. Guillon and Y. Garault, “Accurate Resonant Frequencies of Dielectric Resonators”, IEEE Transactions on Microwave Theory and Techniques, 25, 916 (1977).

[31] A. Serpengüzel, S. Arnold and G. Griffel, “Photonic atoms: Enhanced light coupling’’ in ‘’Microcavities and photonic bandgaps: Physics and applications,’’ J. Rarity and C. Weisbuch, Eds., Kluwer Academic Publishers, Netherlands (1995).

[32] H. Zimmermann, “Integrated Silicon Optoelectronics,” Springer, Berlin (2000).

[33] L. Pavesi and D. J. Lockwood, “Silicon Photonics,” Springer, Berlin (2004).

[34] A. Liu, H. Rong, and D. Hak, "Net Optical Gain in a Low Loss Silicon-on-Insulator Waveguide by Stimulated Raman Scattering," Opt. Express 12, 4261 (2004).

[35] H. Rong, A. Liu, R. Jones, O. Cohen, D. Hak, R. Nicolaescu, A. Fang and M. J. Paniccia, "An All-Silicon Raman Laser," Nature, 433, 292 (2005).

[36] O. Boyraz and B. Jalali, “Demonstration of directly modulated silicon Raman laser,” Opt. Express, 13, 796 (2005).

[37] H. Rong, R. Jones, A. Liu, O. Cohen, D. Hak, A. Fang, and M. J. Paniccia, "A Continuous-Wave Raman Silicon Laser," Nature, 433, 725 (2005).

[38] K. Preston, P. Dong, B. Schmidth, M. Lipson, ‘’High-speed all-optical modulation using polycrystalline silicon microring resonator,’’ Appl. Physics Lett. 92, 151104 (2008)

[39] G.T. Reed and A. P. Knights, ‘’Silicon photonics,’’ Wiley, West Sussex (2004).

[40] R.A. Soref and B.A. Bennett, ‘’Electrooptical effects in Silicon,’’ IEEE J. Quantum Electron. 23, 123 (1987).

[41] M. Lipson, ‘’Switching light on a silicon chip,’’ Opt. Mat., 27, 731 (2005).

[42] N. Grote and H. Venghaus, ‘’Fiber Optic Communication Devices,’’ Springer, Germany (2001)

[43] I.A. Glover, S.R. Pennock, P.R. Sheprherd, ‘’Microwave, devices, circuits and subsystems for communication engineering,’’ Wiley, New York (2005).

[44] Ms. Thesis, Ulaş Kemal Ayaz, ‘’Electrooptical Charecterization of Silicon Microsphere,’’Boğaziçi University, (2006).